**Numerical Heat Transfer- Part A: Applications**

(An International Journal of Computation and Methodology)

https://www.tandfonline.com/journals/unht20

Impact factor = 2.569

Accepted March 9th 2023

# RSM-BASED SENSITIVITY ANALYSIS OF HYBRID NANOFLUID IN AN ENCLOSURE FILLED WITH NON-DARCY POROUS MEDIUM BY USING LBM

***K. Venkatadri[1], Hakan F. Öztop[2*], V. R. Prasad[3], S. Parthiban[3] and O. Anwar Bég[4]***

*[1]Department of Mathematics, Indian Institute of Information Technology Sri City, Chittoor-517464, A.P., India.*

*[2]Department of Mechanical Engineering, Technology Faculty, Fırat University, Elâzığ, Turkey.*

*[3]Department of Mathematics, School of Advanced Sciences, Vellore Institute of technology, Vellore -632014, India.*

*[4]Professor and Director- Multi-Physical Engineering Sciences Group, Aeronautical/Mechanical Engineering, Salford University, School of Science, Engineering and Environment (SEE), Manchester, M54WT, UK.*

****Corresponding Author: E-mail: hfoztop1@gmail.com***

## Abstract

The present analysis is performed to investigate the free convection MHD non-Darcy flow in hybrid nanofluid ($TiO_2$/Cu-water) occupying a differentially heated square closed space. The non-dimensional governing equations for mass, momentum and energy are solved under boundary conditions by using the D2Q9-based Lattice Boltzmann Method. A key novelty of the work is the inclusion of an RSM-based sensitivity analysis. The current investigation has been done considering the variation in Rayleigh number ($10^3 \leq Ra \leq 10^6$), Darcy number ($0.0001 \leq Da \leq 0.1$) and Hartmann number ($0 \leq Ha \leq 50$). It has been shown that the diagonal length of an eddy is boosted as the Rayleigh number increases. In addition, it has been shown that the Nusselt number tends to drop as Ha values rise. From RSM, high Darcy parameter, low volumetric fraction and low Hartmann number are identified as the optimum functioning conditions for heat transfer rates.

**Keywords:** *Magnetic field; porous medium; heat transfer; hybrid nanofluid; Sensitivity analysis; Lattice Boltzmann Method.*

## Nomenclature

| | |
|---|---|
| $B_0$ | Magnetic field intensity (Tesla) |

| | |
|---|---|
| $C_p$ | Specific heat capacity (J/kgK). |
| $C$ | Speed of lattice (m/s) |
| $c_i$ | Discrete particle speed (m/s) |
| Da | Darcy number |
| $P$ | Pressure. (N $m^{-2}$) |
| $Nu$ | Local Nusselt number |
| $f^{eq}$ | Functions of equilibrium density distribution |
| $g^{eq}$ | Equilibrium internal energy distribution. (K) |
| $k$ | Thermal conductivity (W/mK) |
| $f$ | Functions of density distribution. $\left(kg\ m^{-1}\right)$ |
| $L$ | Width (m) |
| $Ra$ | Rayleigh number |
| $n$ | Lattices in the x direction |
| $g$ | Gravitational acceleration (m $s^{-2}$) |
| $Ha$ | Hartmann (magnetic) number. |
| $L_{ref}$ | Cavity length (m) |
| $T$ | Temperature. (K) |
| $u(U,V)$ | Velocity components (m $s^{-1}$) |
| $x(\mathrm{X},\mathrm{Y})$ | Lattice coordinates (m) |
| | ***Greek Symbols*** |
| $\Delta$ | Difference |
| $\Delta x$ | Spacing between lattices. (m) |
| $\alpha$ | Thermal diffusivity. ($m^2$ $s^{-1}$) |
| $\Delta t$ | Time increment. (s) |
| $\mu$ | Dynamic viscosity. (k g $m^{-1}$ $s^{-1}$) |
| $\phi$ | Volumetric fraction |
| $\theta$ | Non-dimensional temperature |
| $\sigma$ | Electrical conductivity. ($Sm^{-1}$) |
| $\tau_\alpha$ | Flow-related relaxation time. (s) |
| $\tau_v$ | Relaxation time for temperature. (s) |

| | |
|---|---|
| $\rho$ | Density. (kg $m^{-3}$) |
| $\nu$ | Kinematic viscosity. ($m^2$ $s^{-1}$) |
| $\omega_i$ | Weighting factor for flow |

***Subscripts***

| | |
|---|---|
| hnf | Hybrid nanofluid |
| C | Cold |
| $H$ | Hot |
| $bf$ | Base fluid |
| F | Fluid |
| nf | Nanofluid |

## 1. Introduction

Heat transfer in porous media has extensive applications in diverse thermal engineering systems. Thermal transport in a heated cavity filled with a porous medium also plays a significant role in various technologies, such as filtration, the disposal of nuclear waste, biochemical reactor processing, geothermics, ink-jet printing, electronic cooling, food processing, energy storage, hybrid fuel cells, heat exchangers and many other areas [1-8]. Nowadays, magnetohydrodynamic (MHD) convection which exploits the electro-conductive properties of certain fluids, is also widely used in electromagnetic materials processing, nano-magnetics, biomagnetic analysis devices and other systems [9-12]. A focused review of selective literature is addressed below of the works on magnetic fields, hybrid nanofluids, thermal/flow field visualization and RSM-based sensitivity analysis as a background of the present work. Thermal convection in an enclosure in the presence of an external magnetic field and thermal buoyancy force has been studied by several researchers [18-22] for controlling heat transfer by suspending nanoparticles in base fluids. Many metallic nanoparticles have been addressed [13-16]. These studies have considered both unitary (single nanoparticle) and hybrid (multiple distinct nanoparticle) nanofluids. Muneeshwaran et al. [17] discussed in detailed the role of hybrid nanofluid in enhancement of heat transport. Rahimi et al. [23] used the lattice Boltzmann technique to examine natural convection in a cuboid enclosure filled with CuO-water nanofluid and concluded that the mean Nusselt number increases as the Rayleigh number increases and that with increment in Rayleigh number, a greater proportion of heat energy is absorbed by the circulation. Khan et al. [24] reported a Lattice Boltzmann simulation of natural

convection of hybrid nanofluid flow in an enclosure with the aspect ratios of 1, 2 and 0.5. They also examined entropy generation within various enclosures (square and rectangular). Hasan et al. [25] examined the natural convection of Cu-water nanofluid in a square enclosure filled with non-Darcy porous medium by using a multi relaxation time-based Lattice Boltzmann method (MRT-LBM). They simulated two different heat loading cases i. e. uniform temperature and sinusoidal temperature distributions and showed that regardless of Darcy number, higher thermal Rayleigh number boosted the Nusselt number. Safaei et al. [26] presented a numerical investigation of natural convection in a shallow enclosure filled with water based $Al_2O_3$ nanofluid under the influence of thermal radiation using a D2Q9 Lattice Boltzmann method. Ghalambaz et al. [27] studied the conjugate convective flow of hybrid nanofluid (Ag-MgO) in an enclosure filled with porous medium in the local thermal non-equilibrium regime. In their study, the heat transfer rate was shown to increase with enclosure height. In addition, a similar analysis was conducted with a finite element method [28]. Hybrid nanofluid convection in a packed bed phase change material was explored by Selimefendigil et al. [35] who also investigate the effects of wind and a magnetic field in a 3D cavity with ventilation ports. Lattice Boltzmann method simulations of double-diffusive convection in closed geometries were explored by Kumar et al. [36]. *Nanofluids* as a new generation of nanoscale engineered fluent media have attracted a lot of research interest and have often been used in conjunction with other heat transfer enhancement techniques such as phase change materials (PCMSs)- see references [37-40]. There is growing evidence that nanofluids are more suitable for various heat transfer applications than conventional fluids. Many researchers have identified that one of the most important parameters in the thermal behavior of such fluids is the *type of nanoparticle* dispersed in the base fluid. [41-44] These investigations showed that nanofluids in combination with phase change materials and with internal geometric modifications in enclosures offer more advantages than other energy storage methods. [44-47]. These approaches are particularly beneficial in solar collector systems [48]. Further studies have explored rheological behaviour of hybrid carbon nanotube/titania nanofluids using RSM and artificial neural network (ANN) methodologies [49] (in which the algorithm is trained in such a way as to be able to automatically modify the input values and to estimate the largest heat transfer), ferromagnetic hybrid nanofluids in enclosures [50], thermal optimization in cavities with LBM and ANN techniques [51], magnetic rheological nanofluids in enclosures [52], mixed convection [53, 54] and oscillatory stratified convection flows [55].

A scrutiny of the literature has identified however, that *magnetohydrodynamic (MHD) natural convention in a differential heated square chamber containing a non-Darcy porous medium saturated with hybrid nanofluid has not been examined thus far* with a D2Q9-based lattice Boltzmann computational approach [56]. This is the novelty and focus of the current article. Additionally, in the present work an RSM sensitivity analysis is also performed to optimize thermal characteristics and hybrid $TiO_2$-Cu/water nanofluid is considered. Detailed visualization of the thermal and flow characteristics is included and validation with earlier studies is also described. The current study has applications in emerging hybrid nano-magnetic fuel cell technologies and also electromagnetic nano-materials processing systems.

## 2. Physical Model

**Fig. 1** presents the physical model to be simulated. The square enclosure is packed with non-Darcy porous medium saturated with magnetic hybrid titanium oxide-copper-water nanofluid and the horizontal walls (top and bottom) are both adiabatic, while the side walls are kept at temperatures of $T_H$ and $T_C$, respectively. A static external magnetic field, $B_o$, is applied.

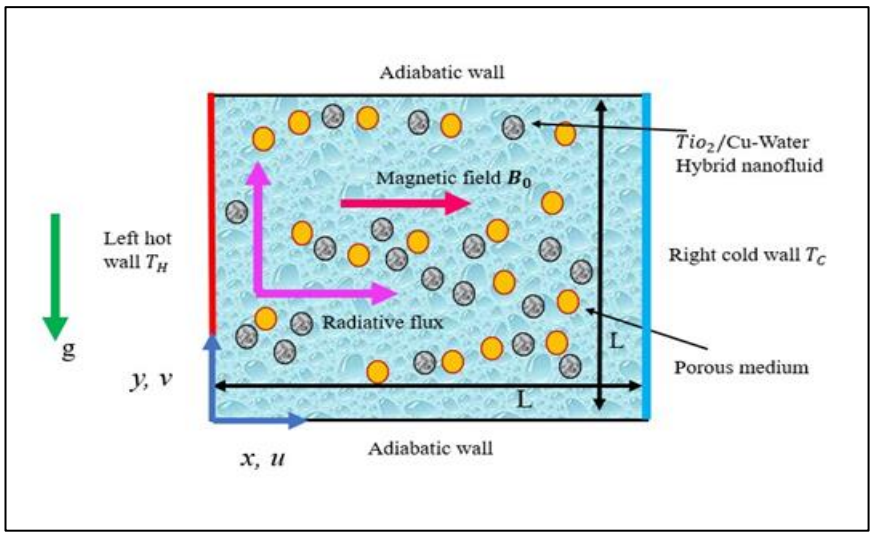


**Fig 1.** Schematic diagram of physical domain.

## 3. Mathematical Formulations

The unsteady laminar incompressible flow of MHD non-Darcy flow of hybrid nanofluids in an enclosure are examined through the partial differential equations as follows- see Refs. [2,5,29, 56]- under a general inclined magnetic field, orientated at angle $\gamma$ to the horizontal.

$$\frac{\partial \bar{u}}{\partial \bar{x}}+\frac{\partial \bar{v}}{\partial \bar{y}}=0 \tag{1}$$

$$\left[\frac{\partial \bar{u}}{\partial \bar{t}}+\bar{u}\frac{\partial \bar{u}}{\partial \bar{x}}+\bar{v}\frac{\partial \bar{u}}{\partial \bar{y}}\right]=-\frac{1}{\rho_{hnf}}\frac{\partial \bar{p}}{\partial \bar{x}}+\nu_{hnf}\left(\frac{\partial^2 \bar{u}}{\partial \bar{x}^2}+\frac{\partial^2 \bar{u}}{\partial \bar{y}^2}\right)+\frac{\sigma_{hnf}}{\rho_{hnf}}B_0^2(\bar{v}sin\gamma cos\gamma-\bar{u}sin^2\gamma)$$

$$-\frac{1.75}{\sqrt{150}}\frac{\rho}{k^{1/2}}\bar{u}\sqrt{\bar{u}^2+\bar{v}^2}-\frac{\nu_{hnf}}{K}\bar{u} \tag{2}$$

$$\left[\frac{\partial \bar{v}}{\partial \bar{t}}+\bar{u}\frac{\partial \bar{v}}{\partial \bar{x}}+\bar{v}\frac{\partial \bar{v}}{\partial \bar{y}}\right]=-\frac{1}{\rho_{hnf}}\frac{\partial \bar{p}}{\partial \bar{y}}+\nu_{hnf}\left(\frac{\partial^2 \bar{v}}{\partial \bar{x}^2}+\frac{\partial^2 \bar{v}}{\partial \bar{y}^2}\right)-\frac{\nu_{hnf}}{K}\bar{v}-\frac{1}{k^{1/2}}\bar{v}\sqrt{\bar{u}^2+\bar{v}^2}\,\frac{1.75}{\sqrt{150}}$$

$$+\frac{(\rho\beta)_{hnf}}{\rho_{hnf}}g(\bar{\theta}-\theta_c)+\frac{\sigma_{hnf}}{\rho_{hnf}}B_0^2(\bar{u}sin\gamma cos\gamma-\bar{v}cos^2\gamma) \tag{3}$$

$$\frac{1}{\alpha_{hnf}}\left(\frac{\partial \bar{\theta}}{\partial \bar{t}}+\bar{u}\frac{\partial \bar{\theta}}{\partial \bar{x}}+\bar{v}\frac{\partial \bar{\theta}}{\partial \bar{y}}\right)=\left(\frac{\partial^2 \bar{\theta}}{\partial \bar{x}^2}+\frac{\partial^2 \bar{\theta}}{\partial \bar{y}^2}\right) \tag{4}$$

All the dimensionless parameters in the governing Equations (1) - (4) are written in the notation section following by below.

$$x=\frac{\bar{x}}{L_{ref}},\ y=\frac{\bar{y}}{L_{ref}},\ v=\frac{\bar{v}L_{ref}}{\alpha_f},\ t=\frac{\bar{t}\alpha_f}{L_{ref}^2},\ p=\bar{p}\frac{L_{ref}^2}{\rho{\alpha_f}^2},\ u=\frac{\bar{u}L_{ref}}{\alpha_f}$$

$$\theta=\frac{\bar{\theta}-\theta_C}{\theta_H-\theta_C},\ Ra=\frac{gB_f q"\Delta\theta L_{ref}^4}{\nu_f\alpha_f k_f},\quad \Pr=\frac{\nu_f}{\alpha_f},\ \alpha_f=\frac{k_f}{(\rho C_P)},\ \Delta\theta=\frac{q"L_{ref}}{k_f}$$

$$Ha=B_0L_{ref}\sqrt{\frac{\sigma_f}{\mu_f}},\ Da=\frac{K}{L_{ref}^2},\ Fc=-\frac{1.75}{\sqrt{150}},\ \Delta T=\frac{q"H}{k_f} \tag{5}$$

Here *u*, *v* are non-dimensional velocity components, *x, y* are the dimensionless , Rayleigh number *Ra*, α is thermal diffusivity, *p* is non- dimensional pressure, $\bar{x},\bar{y}$ are coordinates, *t* is time, *Ha* is Hartmann number, $\mu_{hnf}$ is the dynamic velocity of hybrid nanofluid, *Fc* is the Forchheimer drag coefficient, Pr is Prandtl number, $\sigma_{hnf}$ is hybrid nanofluid of the electrical conductivity, *Da* is Darcy number and $\theta$ is dimensionless temperature."

The changes in heat transfer rate at the horizontal boundaries can be calculated with a local Nusselt number. On the heated wall side, this takes the form:

$$Nu = \frac{k_{nf}}{k_f}\left(\frac{\partial \theta}{\partial X}\right)_{x=1} \tag{6}$$

The related *mean Nusselt number* to be evaluated by integrating the temperature along the hot wall and cold wall:

$$Nu_{ave} = \int_0^L \frac{\partial \theta}{\partial X} dy \tag{7}$$

Using the scaling variables in Eqn. (5), the non-dimensional governing equations emerge as below:

$$\frac{\partial u}{\partial x} + \frac{\partial v}{\partial y} = 0 \tag{8}$$

$$\frac{\partial u}{\partial t} + u\frac{\partial u}{\partial x} + v\frac{\partial u}{\partial y} = -\frac{\partial p}{\partial x} + \boldsymbol{Pr}\left(\frac{\mu_{hnf}}{\mu_f}\right)\left(\frac{\rho_f}{\rho_{hnf}}\right)\left(\frac{\partial^2 u}{\partial x^2} + \frac{\partial^2 u}{\partial y^2}\right) - \frac{1.75}{\sqrt{150}}\frac{u\sqrt{u^2+v^2}}{\sqrt{Da}}$$
$$+\boldsymbol{Ha}^2\boldsymbol{Pr}\left(\frac{\sigma_{hnf}}{\sigma_f}\right)\left(\frac{\rho_f}{\rho_{hnf}}\right)\left(v\,\boldsymbol{sin}\,\gamma\,\boldsymbol{cos}\,\gamma - u\,\boldsymbol{sin}^2\gamma\right) - \frac{\boldsymbol{Pr}}{Da}\left(\frac{\mu_{hnf}}{\mu_f}\right)\left(\frac{\rho_f}{\rho_{hnf}}\right)u \tag{9}$$

$$\frac{\partial v}{\partial t} + u\frac{\partial v}{\partial x} + v\frac{\partial v}{\partial y}$$
$$= -\frac{\partial p}{\partial y} + Pr\left(\frac{\mu_{hnf}}{\mu_f}\right)\left(\frac{\rho_f}{\rho_{hnf}}\right)\left(\frac{\partial^2 v}{\partial x^2} + \frac{\partial^2 v}{\partial y^2}\right) + \left(\frac{(\rho\beta)_{hnf}}{\rho_{hnf}\beta_f}\right)Ra\,Pr\,\theta$$
$$-\frac{Pr}{Da\left(\frac{\mu_{hnf}}{\mu_f}\right)\left(\frac{\rho_f}{\rho_{hnf}}\right)}$$
$$+\mathrm{Ha}^2\mathrm{Pr}\left(\frac{\sigma_{hnf}}{\sigma_f}\right)\left(\frac{\rho_f}{\rho_{hnf}}\right)(u\,sin\gamma cos\gamma - v\,cos^2\gamma) - \frac{1.75}{\sqrt{150}}\frac{v\sqrt{u^2+v^2}}{\sqrt{Da}} \tag{10}$$

$$\frac{\partial \theta}{\partial t} + u\frac{\partial \theta}{\partial x} + v\frac{\partial \theta}{\partial y} = \left(\frac{\partial^2 \theta}{\partial x^2} + \frac{\partial^2 \theta}{\partial y^2}\right)\frac{\alpha_{hnf}}{\alpha_f} \tag{11}$$

The following boundary value conditions govern the solution of the previous system:

$$u = 0,\quad v = 0,\quad \theta = 0 \qquad \text{at } t = 0 \text{ everywhere at } t > 0$$

$$u = 0,\quad v = 0,\quad \frac{\partial \theta}{\partial y} = 0 \qquad \text{for } y = 0, L \text{ and } 0 \le x \le L \tag{12}$$

$\theta = \theta_h, \quad u = 0, \ v = 0$ for $x = 0$ and $0 \le y \le L$

$\theta = \theta_c, \ u = 0, \ v = 0$ for $y = L$ and $0 \le x \le L$ .

In the simulations, the special case of a transverse magnetic field ($\gamma$ = 0) is considered.

### 3.2. Hybrid Nanofluid Properties

Mathematical formulations for water / $TiO_2$ nanofluid and hybrid nanofluid water - Ti $O_2$/Cu are given in the following equations:

$$\rho_{nf} = (1-\phi)\rho_{bf} + \phi\rho_p \tag{13}$$

$$\rho_{hnf} = \phi_{Tio_2}\rho_{Tio_2} + \phi_{Cu}\rho_{Cu} + (1-\phi)\rho_{bf} \tag{14}$$

here $\phi$ is the volumetric friction which is evaluate as; $\phi = \phi_{Tio_2} + \phi_{Cu}$

The nanofluid thermal heat capacity and hybrid nanofluid thermal heat capacity Eq. (16) have been computed following [30,31] as,

$$(\rho C_p)_{nf} = \phi(\rho C_p)_p + (1-\phi)(\rho C_p)_{bf} \tag{15}$$

$$(\rho C_p)_{hnf} = \phi_{Tio_2}(\rho C_p)_{Tio_2} + \phi_{Cu}(\rho C_p)_{Cu} + (1-\phi)(\rho C_p)_{bf} \tag{16}$$

The coefficient of thermal expansion for nanofluid can be obtained via the formula:

$$(\rho\beta)_{nf} = \phi(\rho\beta)_p + (1-\phi)(\rho\beta)_{bf} \tag{17}$$

Therefore, the thermal expansion can be characterised as

$$(\rho\beta)_{hnf} = \phi_{Tio_2}(\rho\beta)_{Tio_2} + \phi_{Cu}(\rho\beta)_{Cu} + (1-\phi)(\rho\beta)_{bf} \tag{18}$$

The nanofluid thermal diffusivity ( $\alpha_{nf}$ ) is defined as

$$\alpha_{nf} = \frac{k_{nf}}{(\rho C_p)_{nf}} \tag{19}$$

The thermal conductivity of the nanofluid is represented in equation (19) by Maxwell-Garnetts model, as shown below.

$$\frac{k_{nf}}{k_{bf}} = \frac{\left(2k_{bf} + k_p\right) - \left(k_{bf} - k_p\right)2\phi}{\left(2k_{bf} + k_p\right) - \phi\left(k_{bf} - k_p\right)} \tag{20}$$

Thus, the thermal diffusivity of the hybrid nanofluid can be described by:

$$\alpha_{hnf} = \frac{k_{hnf}}{\left(\rho C_p\right)_{hnf}} \tag{21}$$

The hybrid nanofluid thermal conductivity is also evaluated using the Maxwell-Garnetts model, as show below:

$$\begin{aligned}\frac{k_{hnf}}{k_{bf}} = &\left( \frac{\left(\phi_{Tio_2} k_{Tio_2} + \phi_{Cu} k_{Cu}\right)}{\phi} + 2k_{bf} + 2\left(\phi_{Tio_2} k_{Tio_2} + \phi_{Cu} k_{Cu}\right) - \left(2\phi k_{bf}\right) \right) \\ &\times \left( \frac{\left(\phi_{Tio_2} k_{Tio_2} + \phi_{Cu} k_{Cu}\right)}{\phi} + 2k_{bf} - \left(\phi_{Tio_2} k_{Tio_2} + \phi_{Cu} k_{Cu}\right) + \left(\phi k_{bf}\right) \right)\end{aligned} \tag{22}$$

The nanofluid dynamic viscosity is based on the Brinkman model - Ref. [32]

$$\mu_{nf} = \frac{\mu_{bf}}{\left(1-\phi\right)^{2.5}} \tag{23}$$

Here $\mu_{bf}$ is the viscosity of the base fluid. The effective dynamic viscosity of the hybrid $Tio_2$/Cu -Water nanofluid is:

$$\mu_{hnf} = \frac{\mu_{bf}}{\left(1-(\phi_{Tio_2} + \phi_{Cu})\right)^{2.5}} \tag{24}$$

The *effective electrical conductivity* of a unitary nanofluid is:

$$\frac{\sigma_{nf}}{\sigma_{bf}} = 1 + \frac{3\left(\frac{\sigma_p}{\sigma_{bf}} - 1\right)\phi}{\left(\frac{\sigma_p}{\sigma_{bf}} + 2\right) - \left(\frac{\sigma_p}{\sigma_{bf}} - 1\right)\phi} \tag{25}$$

Therefore, we can calculate the effective electric conductivity of the $Tio_2$/Cu hybrid nanofluid as follows:

$$\frac{\sigma_{hnf}}{\sigma_{bf}} = 1 + \frac{3\left(\frac{\left(\phi_{Tio_2}\sigma_{Tio_2} + \phi_{Cu}\sigma_{Cu}\right)}{\sigma_{bf}} - \left(\phi_{Tio_2} + \phi_{Cu}\right)\right)\phi}{\left(\frac{\left(\phi_{Tio_2}\sigma_{Tio_2} + \phi_{Cu}\sigma_{Cu}\right)}{\phi\sigma_{bf}} + 2\right) - \left(\frac{\left(\phi_{Tio_2}\sigma_{Tio_2} + \phi_{Cu}\sigma_{Cu}\right)}{\sigma_{bf}} - \left(\phi_{Tio_2} + \phi_{Cu}\right)\right)\phi} \quad (26)$$

**Table 1**: Nanoparticles and aqueous base fluid thermophysical properties- Ref. [31]

| **Property** | **Water** | $\boldsymbol{Tio_2}$ | **Cu** |
|---|---|---|---|
| $\rho(\mathrm{kg}m^{-3})$ | 997.1 | 4250 | 8,933 |
| $\beta(k^{-1})$ | $21 \times 10^{-5}$ | $0.9\times 10^{-5}$ | $1.67\times 10^{-5}$ |
| $\mathrm{k}(\mathrm{W}m^{-1}k^{-1})$ | 0.613 | 8.9538 | 401 |
| $\sigma(\Omega^{-1}m^{-1})$ | 0.05 | $2.6 \times 10^{7}$ | $5.96 \times 10^{7}$ |
| $C_p(\mathrm{J}kg^{-1}K^{-1}$ | 4179 | 686.2 | 385 |

## 4. Lattice Boltzmann Method

The unsteady governing Eqs. (8–12) have been solved by the two-dimensional D2Q9 double population function lattice Boltzmann method and approximated using the Bhatnagar-Gross-Krook (BGK) method. In this method, *f (velocity) and g (temperature)* are the two distinct functions. The corresponding $D_2Q_9$ lattice is seen in Fig. 2, based on Ref. [24]. The appropriate equations are:

***fluid field***

$$f_i\left(x + C_i\Delta t, t + \Delta t\right) = f_i\left(x,t\right) + \frac{\Delta t}{\tau_\alpha}\left(f_i\left(x,t\right) - f_i^{eq}\left(x,t\right)\right) + \Delta t F_i \quad (27)$$

***Temperature field:***

$$g_i\left(x + C_i\Delta t, t + \Delta t\right) = g_i\left(x,t\right) - \Delta t\frac{1}{\tau_\alpha}\left(g_i\left(x,t\right) - g_i^{eq}\left(x,t\right)\right) \quad (28)$$

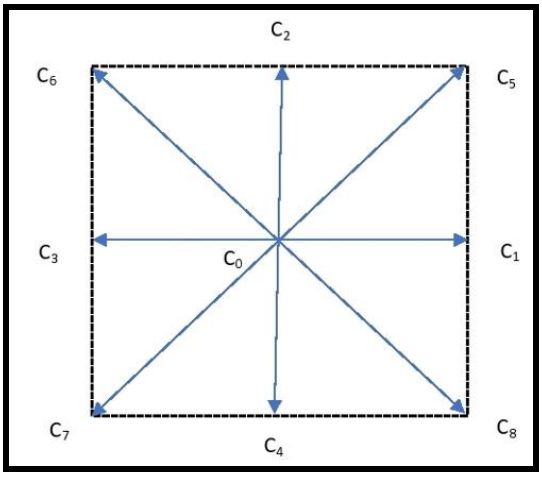


**Fig. 2**: D2Q9 lattice model

In Equations (27, 28), $C_i$ denotes discrete lattice model velocity in the direction *I*, while *x and t* represent time and the spatial location of the fluid node, respectively. Also, $f_i$ is a function representing particle dispersion along different lattice directions, $\Omega$ is the collision operator and $F_i$ is the external force in the direction of lattice velocity.

$$f_i^{eq} = w_i \rho \left[ 1 + \frac{3(C_i u)}{C_S^2} + \frac{9(C_i u)^2}{2C_S^4} - \frac{3u^2}{2C_S^2} \right] \tag{29}$$

$$g_i^{eq} = w_i' T \left[ 1 + 3\frac{C_i u}{C_S^{\ 2}} \right] \tag{30}$$

The thermal model of two populations uses the simulations and these are well-defined with the associated weighting factors as follows:

$$w_i = \begin{Bmatrix} \frac{1}{9} & i = 1,2,3,4 \\ \frac{4}{9} & i = 0 \\ \frac{1}{36} & i = 5,6,7,8 \end{Bmatrix} \tag{31}$$

$$C_i = \begin{Bmatrix} (\pm 1, 0), (0, \pm 1) & \frac{1}{9}, & i = 1,2,3,4 \\ (0,0) & \frac{4}{9}, & i = 0 \\ (\pm 1, \pm 1) & \frac{1}{36}, & i = 5,6,7,8 \end{Bmatrix} \quad (32)$$

Here ν is the kinematic viscosity and α is the thermal diffusivity which are related to the instantaneous relaxation time by a continuous Equation. (31):

$$\nu = \left[\tau_\nu - \frac{1}{2}\right] c_s{}^2 \Delta t \quad , \quad \alpha = \left[\tau_\alpha - \frac{1}{2}\right] c_s{}^2 \Delta t \quad (33)$$

Where $c_s = \frac{c}{\sqrt{3}}$. (34)

The external force, $F_i$ is defined as:

$$F_i = \frac{w_i}{C_S^2} F.C_i \quad (35)$$

The *total external physical force* is given by:

$$F = F_x + F_y \quad (36)$$

LBM defines macroscopical quantities $u$, $\theta$ and $\rho$ as follows:

Density of flow: $\rho = \sum_i f_i$ (37)

Momentum: $\rho u = \sum_i f_i C_i$ (38)

Temperature: $\theta = \sum_i g_i$ (39)

## 5. The validation and grid independence

In order to reduce computational costs and investigate the impact of the mesh size grid independence tests have been performed using MATLAB-based LBM. Five different grid sizes have been investigated in order to make the right choice. Grid size (101 * 101) was determined

to be optimal for continuing the current work based on the results shown in Table 2 and Fig. 2. This is due to the fact that the mean Nusselt number value remains constant after a certain grid size. The research conducted by Ref. [28] supports the findings presented. Table 3 displays the results of the comparison, which ensures confidence in the BM code accuracy.

**Table. 2.** Grid independence test Ra = $10^3$

| Grid Size | (Mean Nu) Present | Ref. Mehryan et al. [33] | Error |
|---|---|---|---|
| 50×50 | 13.388 | 13.392 | |
| 100×100 | 13.567 | 13.569 | 1.32 |
| 150×150 | 13.602 | 13.608 | 0.28 |
| 200×200 | 13.620 | 13.622 | 0.10 |

The grid test is less than 1% percentage error. therefore, the grid during test is 101 * 101. For Nusselt number rightly 1.00, so a grid size test of 101 *101 is accurately used to separate the domain.

**Table. 3.** Compare analysis of Ra vs. Nu.

| Ra | $Nu_{ave}$ | |
|---|---|---|
| | Mehryan et al.[33] | Current study |
| $10^4$ | 2.251 | 2.253 |
| $10^5$ | 4.598 | 4.594 |
| $10^6$ | 8.976 | 8.982 |

## 6. Results and Discussion

The influence of Rayleigh number $10^3 \le Ra \le 10^6$, Darcy number $0.0001 \le Da \le 0.1$, Hartmann number $0 \le Ha \le 100$, streamline, isotherm and local Nusselt number distribution of the differential heated square chamber hybrid nanofluids in MHD natural convection flow

are visualized in **Figs 3-12**. Additionally for further validation the LBM results are compared with the earlier study of Abdelmalek *et al.* [34] in Fig. 3. Very good correlation is observed for the streamline (iso-velocity) and isotherm contours confirming confidence in the accuracy of the LBM code.

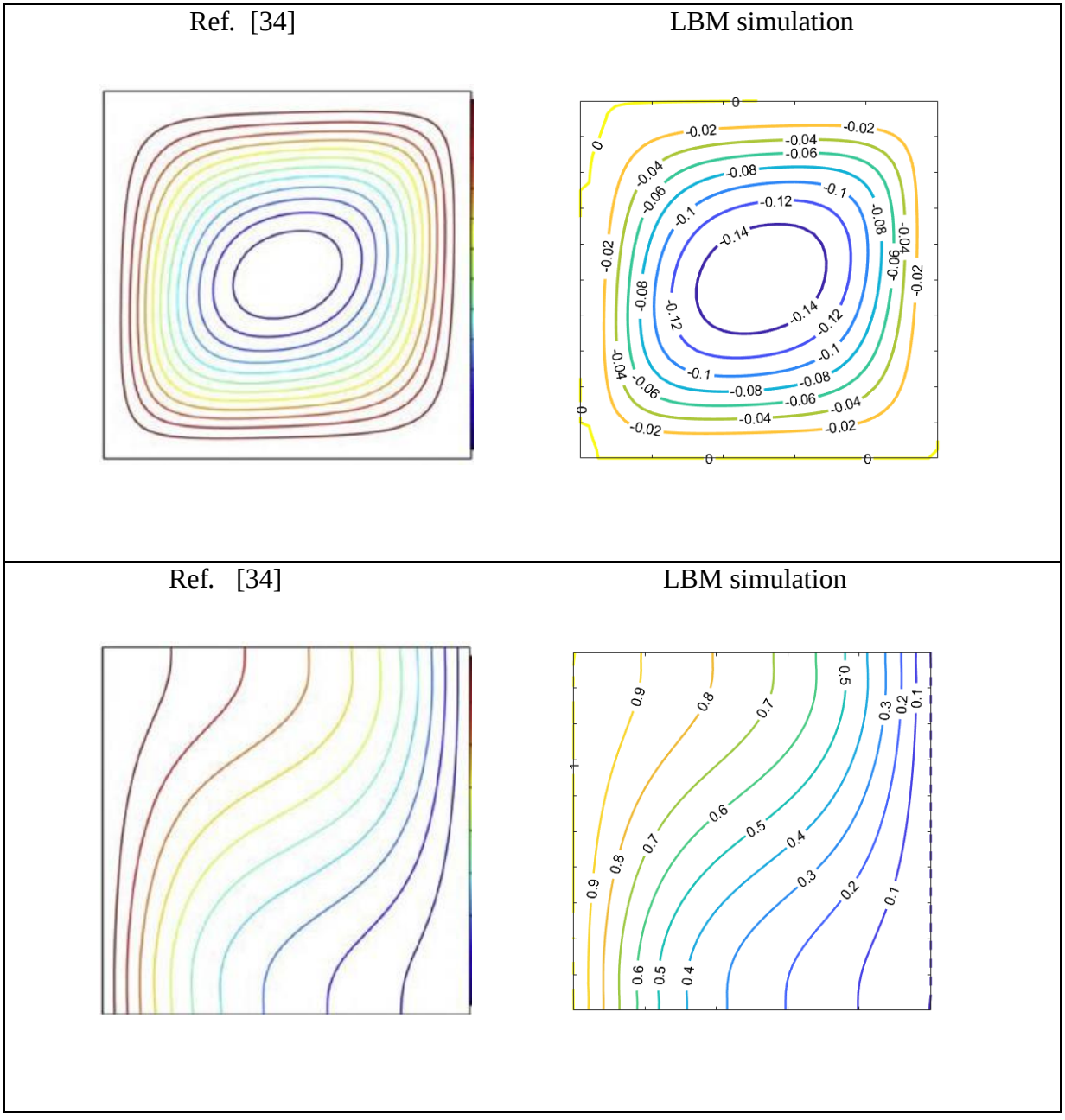


**Fig.3.** Comparison of contour plots for streamlines and isotherms with Abdelmalek *et al.* [34] *for* $Ra = 10^4$, $Da = 0.01$.

The validation in Fig. 3 produces similar results to Ref. [34] with certain changes to the boundary conditions and geometry, but without the magnetic field (i. e. zero Hartmann number) and with infinity Darcy number.

### 6.1 The impact of parameters on thermofluid characteristics

Fig.4. (a-d) depicts the streamlined contours for the $TiO_2$-Cu/water hybrid nanofluids for distinct values of the Rayleigh number. At the lowest Rayleigh number a clockwise rotating vortex is formed in the interior of the enclosure. As the Rayleigh number increases along the horizontal axis, the vorticity grows, resulting in more compact flow close to the horizontal walls, and hence improved heat transfer in the region. The central single vortex bifurcates into two cells with increasing Rayleigh number, and these are significantly skewed with the larger vortex near the left wall and the smaller near the right wall. Thermal buoyancy therefore strongly modifies the internal flow structure and morphs the circulation which is biased towards the left wall.

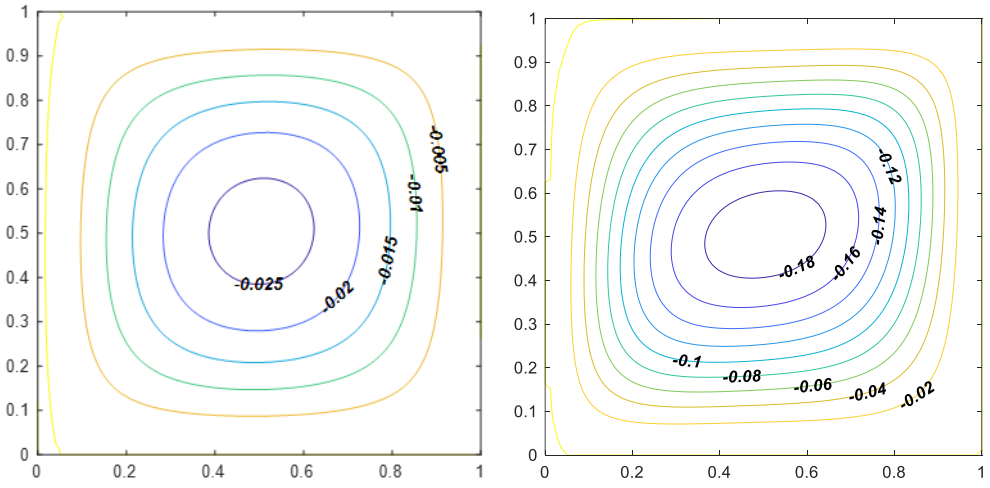


(a) (b)

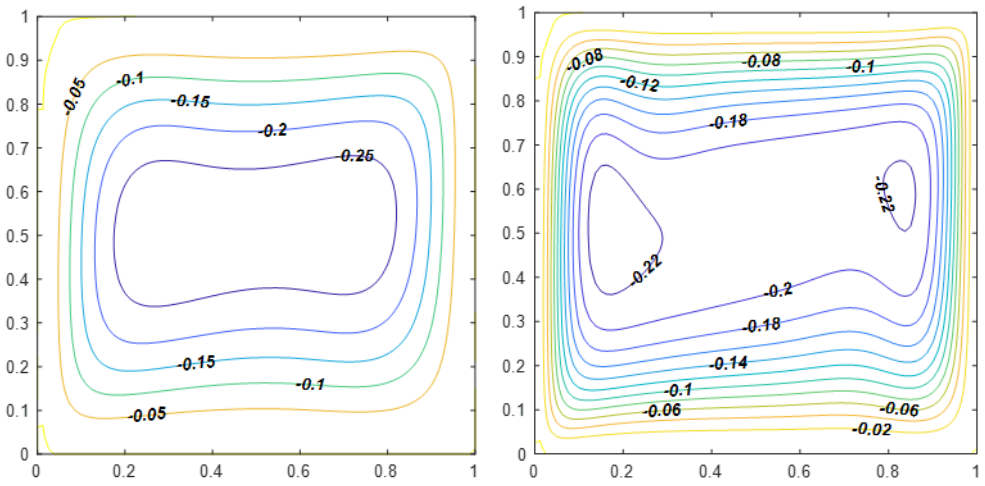


(c) (d)

**Fig.4.** streamlines various for Ra, *with Pr=6.2, Ha=5, Da=0.1.* (a) Ra = $10^3$, (b) Ra=$10^4$, (c) Ra = $10^5$, (d) Ra=$10^6$

Fig.5(a-d) illustrates at lower Rayleigh numbers isotherms run generally parallel to the vertical boundaries. However, with a greater Rayleigh number the isotherms are likewise significantly tilted towards the upper right corner cold wall and the bottom left corner hot wall. Increasing hybrid nanofluid relative to viscous force as simulated in the Rayleigh number clearly significantly modifies both the streamline and isotherm morphologies. Isotherms also become increasingly *sigmoidal* (as Ra increases from $10^5$ to $10^6$) from the lower left corner to the upper right corner and are more prominently compressed against both the left hot wall and right wall. This effect is maximized for the highest Rayleigh number (Ra=$10^6$). Heat transfer within the enclosure is therefore very substantially modified with increase in thermal buoyancy which modifies thermal convection currents to distort both velocity and temperature distributions.

**Fig. 6(a-d)** shows that increasing applied magnetic field (higher Hartmann number) markedly affects the flow and thermal fields within the cavity. First, it apparently suppresses flow intensity. A peanut-like asymmetric vortex lattice is created when magnetic field is absent (zero Hartmann number). With increasing Hartmann number, the elevation in Lorentzian magnetic body force produces an asymmetric oval vortex which migrates towards the lower left and upper right corner of the cavity and is increasingly orientated diagonally. Progressively, the internal circulation is gradually changed, the vortex stretching toward the upper wall and the lower side of the wall and becoming more asymmetric. The streamline contours are

increasingly constricted and this is most prominent at very high Hartmann numbers, in the lower left and upper right corners of the enclosure.

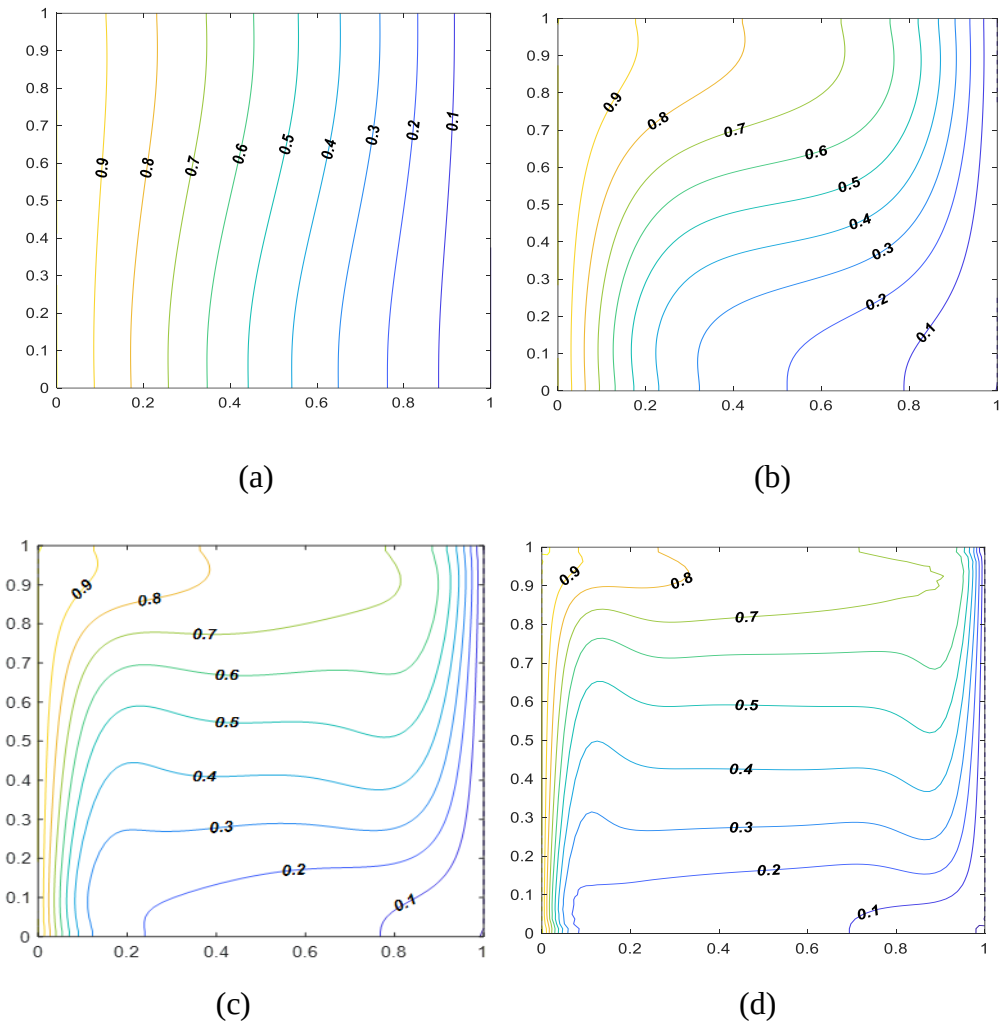


**Fig.5.** isotherms various for Ra, *Pr=6.2*, *Ha=5*, *Da=0.1*. Ra = $10^3$, (b) Ra=$10^4$, (c) Ra = $10^5$, (d) Ra=$10^6$.

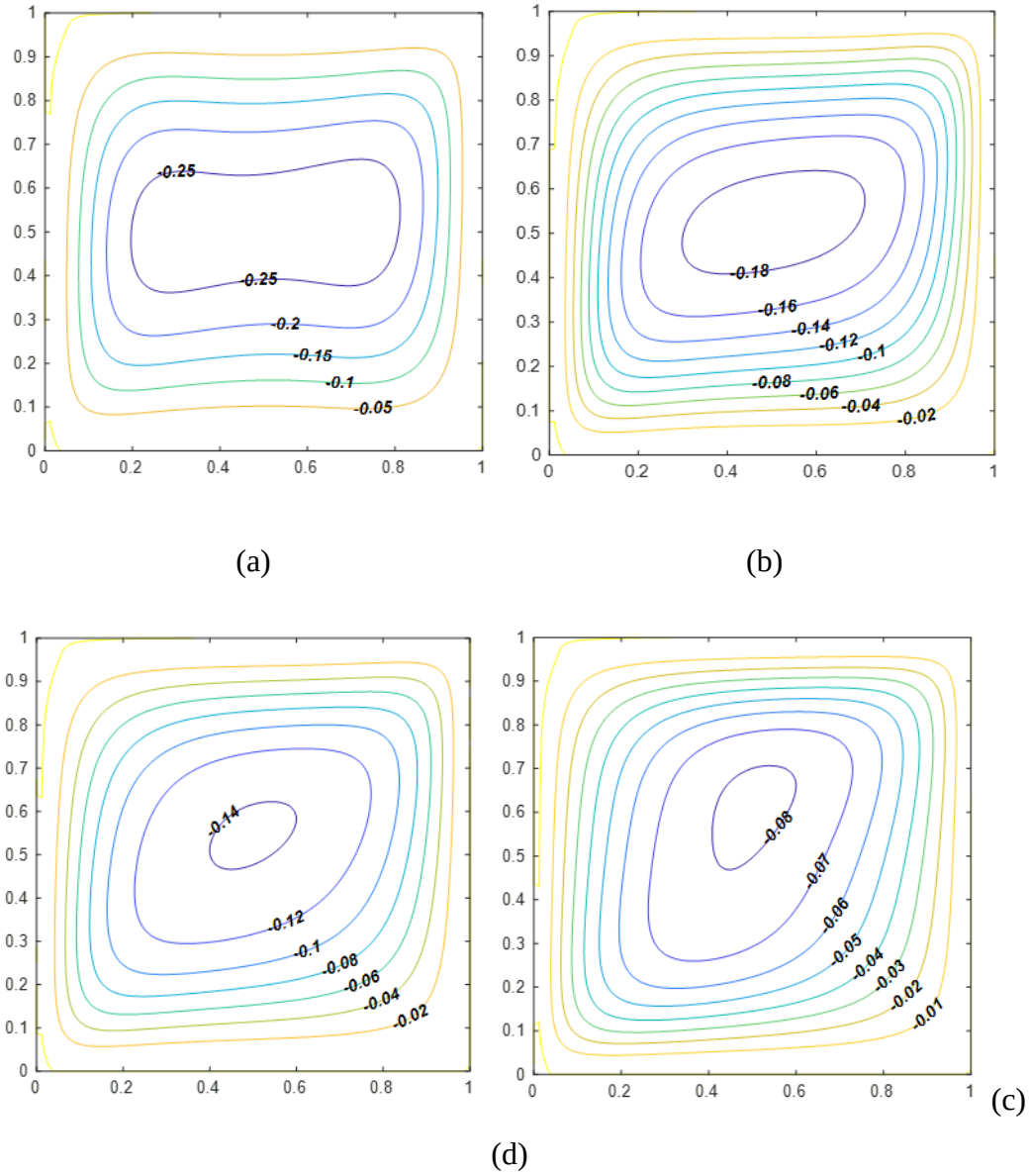


***Fig .6.*** Streamlines for various *(a) Ha = 0, (b) Ha=20, (c) Ha = 30, (d) Ha= 50 with Pr=6.2, Ra = $10^5$, Da=0.1.*

In Figs. 7(a–d), the isotherms are exhibited a sigmoidal structure from the down left side corner to the upper right-side corner of the cavity. The clustering in isotherms towards the left and right walls is also intensified with rising *Ha*. The magnetic field, therefore, increases heat transfer in the regime whereas it suppresses internal circulation i.e., damps the flow. The isotherms on the left and right walls are progressively crowded with increment in *Ha* and there is relaxation at the middle zone, although the sigmoidal topology is preserved. As hybrid nanofluid motion in the enclosure is impeded with the stronger magnetic field, greater work is expended in dragging the hybrid nanofluid against the transverse magnetic field. This is

dissipated as thermal energy and heats the enclosure generating a modification in isotherm contours and boosting temperatures.

Figures 8(a-d) depicted the streamline curves for hybrid $TiO_2$-Cu/water nanofluids for distinct values of Darcy number. With increasing Da values, the single vortex cell is distorted into a peanut structure (dual vortex). As the Darcy number increases along the horizontal axis, the vortices increase in rotation towards the left lower end and the right upper end resulting in an elliptical trajectory in the middle of the horizontal walls in a clockwise direction. The topology is greatly skewed from the lower left to the upper right corners at intermediate Darcy numbers but at higher Darcy number the peanut vortex structure aligns horizontally across the enclosure. As the Darcy number increases (higher permeability of the porous medium), the Darcian and Forchheimer drag forces are reduced in the regime. This modifies strongly the central vorticity and accelerates the flow leading to greater intensity of circulation.

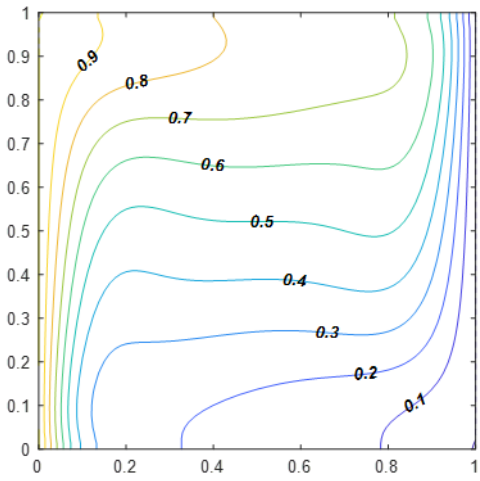


(a)

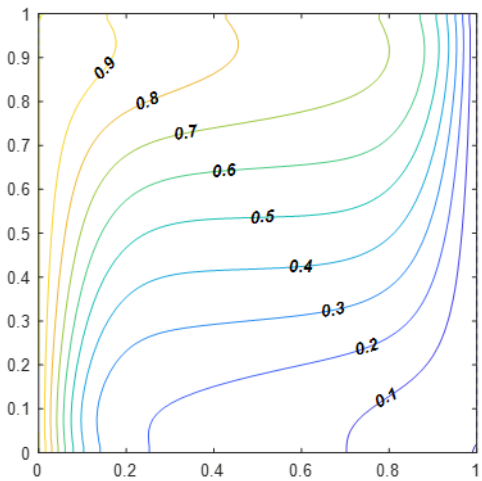


(b)

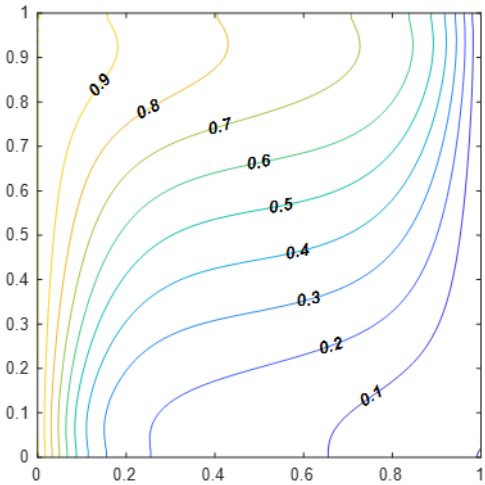


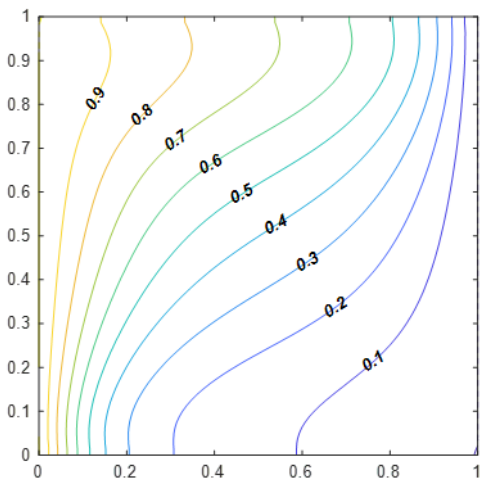

(c) (d)

***Fig 7.*** Isotherms for various *(a) Ha = 0, (b) Ha=20, (c) Ha = 30, (d) Ha= 50 with Pr=6.2, Ra = $10^5$, Da=0.1.*

Fig. 9 (a-d) illustrates that at lower Darcy numbers, isotherms run generally parallel to the vertical boundaries, since the porous medium permeability is smaller and heat conduction between solid fibers is greater. However, with a greater Darcy number the isotherms are significantly tilted towards the upper right corner cold wall and the bottom left corner hot wall. Increasing permeability of the porous medium permits greater percolation space for the hybrid magnetic nanofluid (Darcy number is proportional to permeability) and this clearly significantly modifies both the streamline and isotherm morphologies. Isotherms also become increasingly sigmoidal (high Darcy number value) from the bottom left corner to the upper top corner and are more strongly compressed against both the left hot wall and right wall. This effect is maximized for the highest Darcy number. Heat transfer within the enclosure is therefore very substantially modified with a reduction in the porous drag forces.

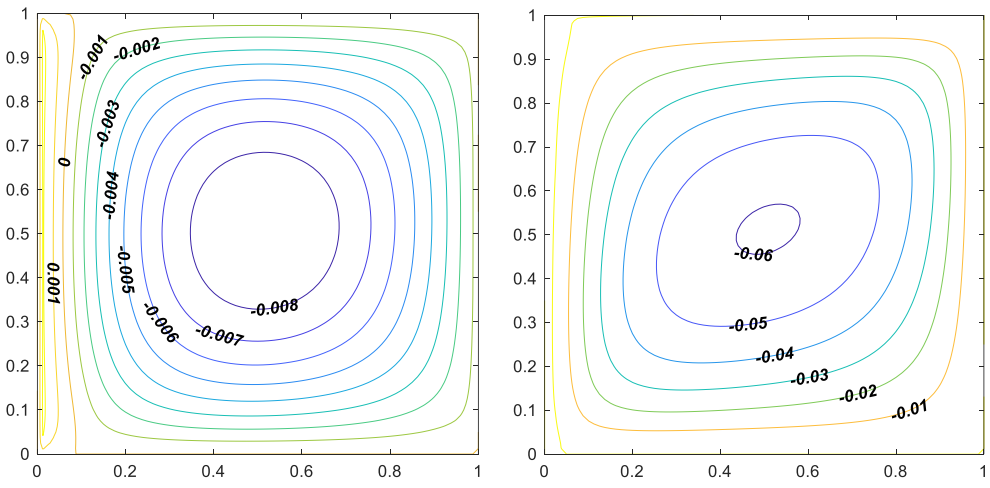


(a) (b)

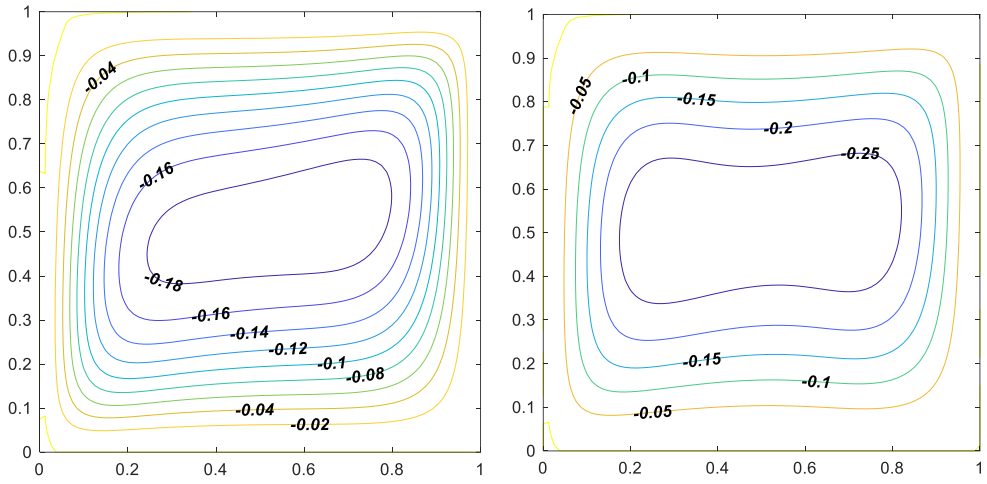


(c) (d)

**Fig *8***. streamlines various for Da, *Pr=6.2*, *Ha=5*, Ra = $10^5$. *(a) Da = 0.0001, (b) Da=0.001, (c) Da = 0.01, (d) Da= 0.1.*

`

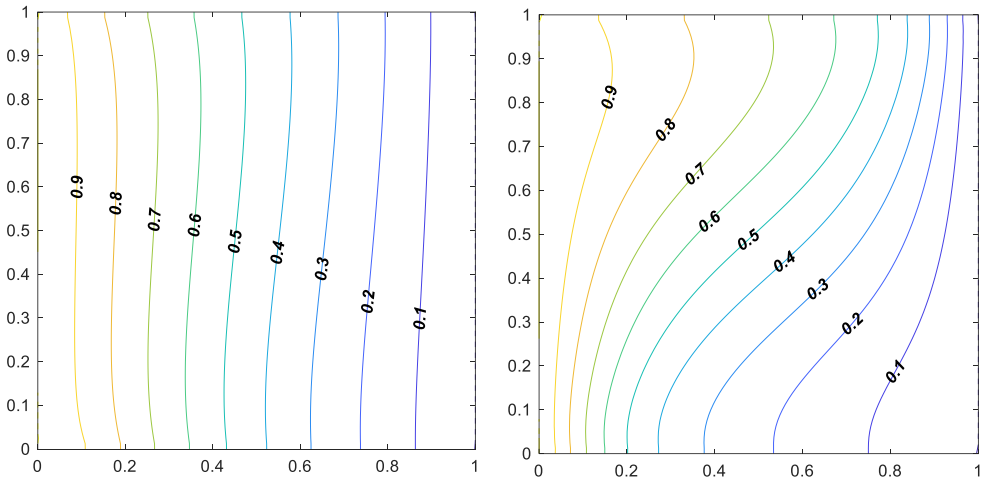


(a) (b)

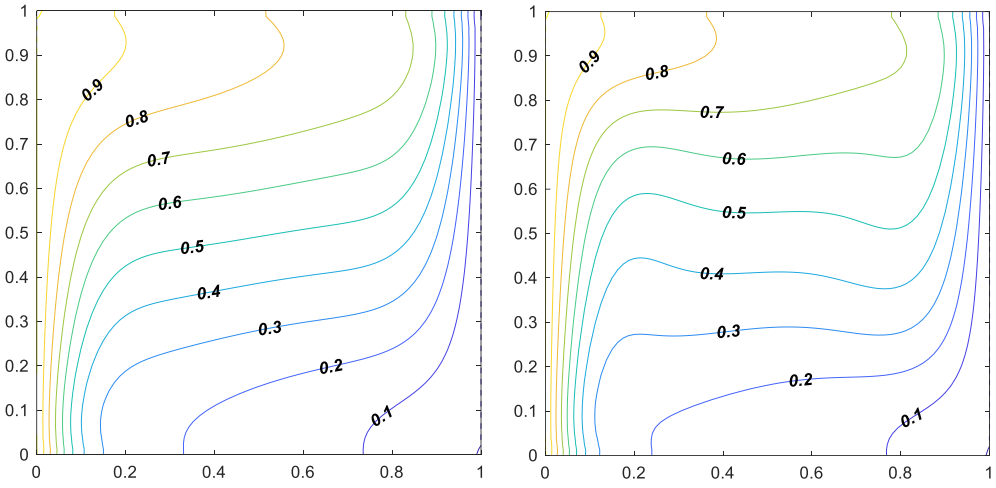


(c) (d)

**Fig** 9. Isotherms various for Da, *Pr=6.2*, *Ha=5*, Ra = $10^5$ *(a) Da = 0.0001, (b) Da=0.001, (c) Da = 0.01, (d) Da= 0.1.*

**Fig.10** demonstrates that raising the Rayleigh number significantly enhances the magnitude of the Nusselt number i. e. thermal buoyancy force progressively elevates heat conveyed to the boundary. The Nusselt number is also boosted as we progress from the upper of the heated left wall to the base of the chamber since the profile changes from a vertical line to a decaying negative slope. This shows that as we go from the top of the cavity to the bottom along the left hot wall, thermal convection rises relative to thermal conduction. Greater heat transmission to the boundary is produced from the magnetic nanofluid in the interior. The temperature difference across the enclosure will inevitably contribute to the natural convection currents in the regime. The wall temperatures can therefore also be manipulated to achieve regulation in the heat transferred to the boundaries.

**Fig.11** shows that as magnetic field intensity is increased i. e. with greater Hartmann numbers, the Nusselt number strongly increases. Since stronger magnetic field generates heat in the regime, there is a boost in heat transfer rate to the wall. Convective currents are also enhanced with magnetic field although the flow is damped. Again, Nusselt number is boosted as one moves from the top of the left heated wall to the bottom. Clearly the external magnetic field can be used to strongly manipulated heat transfer characteristics not only in the interior but also at the boundaries. This is important for thermal management since in fuel cells (and magnetic batch processors), degradation can be induced via thermal fields at the walls leading to

corrosion and other effects. Manipulation of the external magnetic field provides therefore a useful thermal control mechanism.

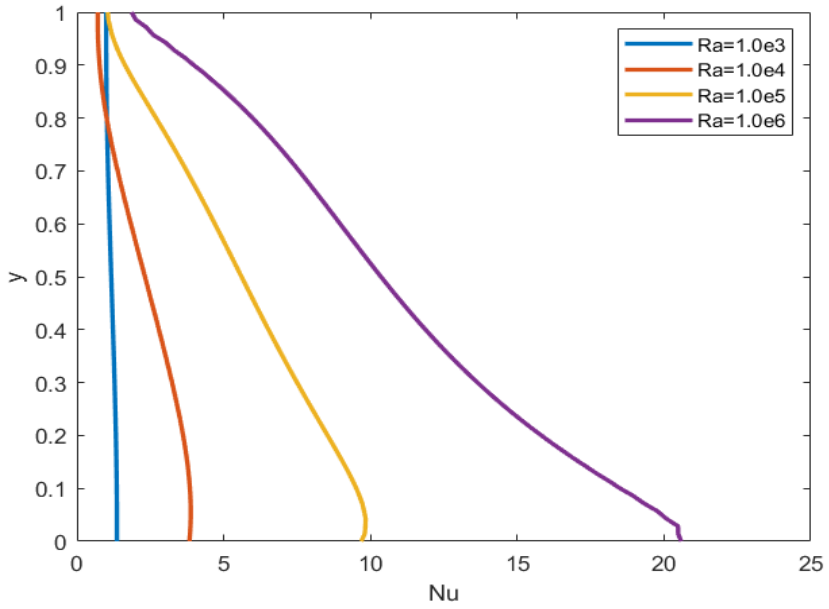


**Fig .10.** Plots of Nu vs. Ra for *Ha = 5, Da = 0.1, Pr = 6.2*

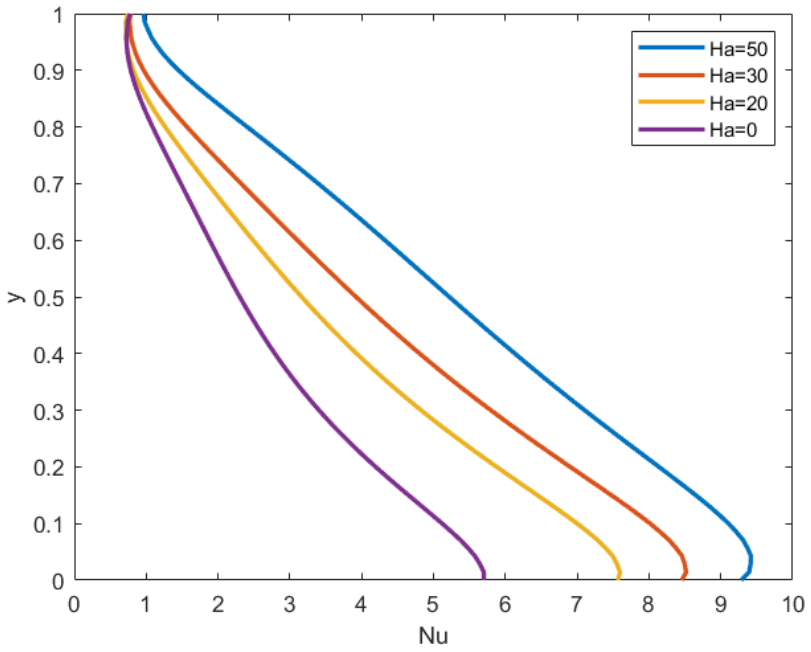


**Fig**. 11. Local Nusselt various Ha for *Da = 0.1, Ra = $10^{5,}$ Pr = 6.2,*

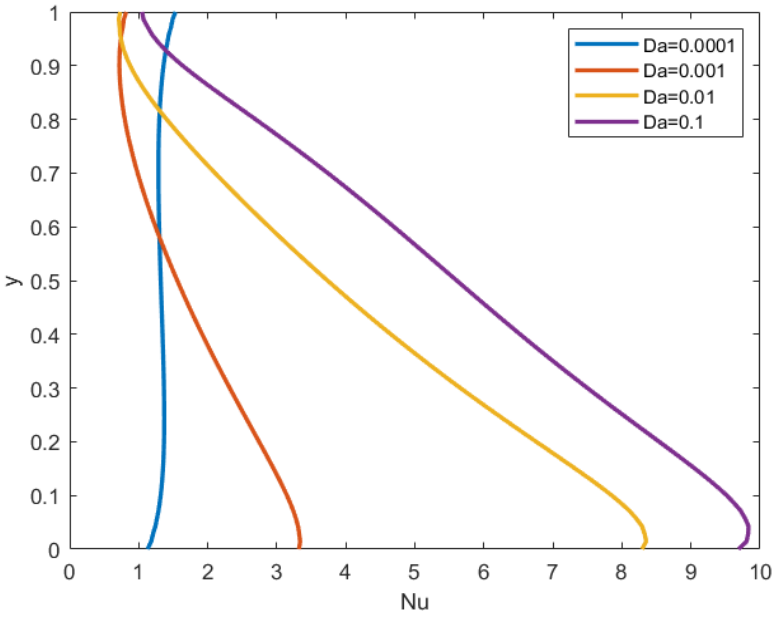


**Fig**. 12. Local Nusselt vs. Da for *Ha =10, Pr = 7, Ra =10*$^5$.

**Fig .12** shows that despite the local Nusselt number initially increasing close to the top hot wall of the left, with a reduction in Darcy number from Da = 0.1, 0.001, and 0.01, with a subsequent reduction to Da = 0.0001, this trend is reversed. Only in the vicinity of the top of the left wall does lower permeability (lower Darcy number) produce a higher Nusselt number. As we further descend along the hot wall, local Nusselt number magnitudes for Da = 0.1 exceed those computed for Da = 0.01. Therefore, further down the boundary, for the highest permeability (the largest value of the Darcy number), the heat transfer rate to the hot wall is generally enhanced. Higher permeability implies lower percentage presence of solid fibers. This contributes greatly to the modification in thermal conduction heat transfer and greater thermal convection afforded to the percolating magnetic hybrid nanofluid at higher Darcy number. Again, the inclusion of a porous medium in the enclosure provides designers with a robust technique for modifying heat transfer to the boundaries.

## 7.Optimization procedure

### 7.1 Response surface methodology *(RSM)* analysis

RSM is a technique for sensitivity analysis [26]. The three principal control factors in the present study, i.e. Hartmann Number (Ha), Darcy parameter (Da) and volumetric fraction ($\phi$) are chosen as RSM parameters specified with (-1) low, (0) medium, and (+1) high levels,

respectively. RSM throws light on the connection between other response variables and factors. The prescribed values of the variables of value is given in Table 4. Using statistical software, the regression equations with quadratic polynomials are studied to determine the coefficients and their impact on transport characteristics e. g. Nusselt number.

**Table.4. Important determinant factors and ranges of values**

| **KEY FACTORS** | **SYMBOLS** | **LEVELS** | | |
|---|---|---|---|---|
| | | **-1** | **0** | **1** |
| | | **(LOW)** | **(MEDIUM)** | **(HIGH)** |
| Ha | X1 | 20 | 30 | 50 |
| Da | X2 | 0.001 | 0.01 | 0.1 |
| $\phi$ | X3 | 0.01 | 0.03 | 0.05 |

The calculated RSM model accuracy is tested using the ANOVA (ANalysis Of VAriance) data in Table5 [25]. As long as the p-value is less than or equal to 0.05, the results are deemed *statistically significant* at 88% confidence interval. The influence of the Darcy number (Da), Hartmann number (Ha), and volumetric fraction ($\phi$ ) on natural convection in the non-Darcy porous medium enclosure is explored. Table 5 shows the dimensionless parameters utilised in this simulation:

**Table.5. The levels of factor values as well as their experimental results for Nu***

| Run order | Code values | | | Values of parameters | | | Nu* |
|---|---|---|---|---|---|---|---|
| | X1 | X2 | X3 | Ha | Da | $\phi$ | |
| 1 | -1 | -1 | -1 | 20 | 0.001 | 0.01 | 3.161313 |
| 2 | 1 | -1 | -1 | 50 | 0.001 | 0.01 | 3.785506 |
| 3 | -1 | 1 | -1 | 20 | 0.1 | 0.01 | 6.04095 |
| 4 | 1 | 1 | -1 | 50 | 0.1 | 0.01 | 3.99039 |
| 5 | -1 | -1 | 1 | 20 | 0.001 | 0.05 | 2.9716 |
| 6 | 1 | -1 | 1 | 50 | 0.001 | 0.05 | 2.700872 |
| 7 | -1 | 1 | 1 | 20 | 0.1 | 0.05 | 5.698121 |

| | | | | | | | |
|---|---|---|---|---|---|---|---|
| 8 | 1 | 1 | 1 | 50 | 0.1 | 0.05 | 3.631295 |
| 9 | -1 | 0 | 0 | 20 | 0.01 | 0.03 | 5.166674 |
| 10 | 1 | 0 | 0 | 50 | 0.01 | 0.03 | 3.619565 |
| 11 | 0 | -1 | 0 | 30 | 0.001 | 0.03 | 2.98724 |
| 12 | 0 | 1 | 0 | 30 | 0.1 | 0.03 | 5.034516 |
| 13 | 0 | 0 | -1 | 30 | 0.01 | 0.01 | 4.753309 |
| 14 | 0 | 0 | 1 | 30 | 0.01 | 0.05 | 4.411888 |
| 15 | 0 | 0 | 0 | 30 | 0.01 | 0.03 | 4.582364 |
| 16 | 0 | 0 | 0 | 30 | 0.01 | 0.03 | 4.582364 |
| 17 | 0 | 0 | 0 | 30 | 0.01 | 0.03 | 4.582364 |
| 18 | 0 | 0 | 0 | 30 | 0.01 | 5 | 4.582364 |
| 19 | 0 | 0 | 0 | 30 | 0.01 | 5 | 4.582364 |
| 20 | 0 | 0 | 0 | 30 | 0.01 | 5 | 4.582364 |

The face-centered CCD - central composite design is utilised for the RSM analysis [25]. The number of the runs in these "experiments" is computed using the formula $2^F + 2F + P$, where N is the number of aspects and P denotes the number of design centre points. The design of the current analysis which has three parts involves eight factorial points, six axial points and six nodes. As shown in Table 5, the numerical experimental design has therefore twenty runs in total which corresponds to nineteen degrees of freedom.

**Table.6. ANOVA data**

| **SOURCE** | **DEGREE OF FREEDOM** | **ADJUSTED SUM OF SQUARES** | **ADJUSTED MEAN SQUARE** | **F-VALUE** | **P-VALUE** |
|---|---|---|---|---|---|
| Model | 9 | 14.6044 | 1.62271 | 16.81 | 0.000 |
| Linear | 3 | 11.3548 | 3.78494 | 39.20 | 0.000 |
| Ha | 1 | 3.5490 | 3.54898 | 36.76 | 0.000 |
| Da | 1 | 7.1748 | 7.17479 | 74.31 | 0.000 |
| Q | 1 | 0.5129 | 0.51293 | 5.31 | 0.044 |
| Square | 3 | 5.4641 | 1.82137 | 18.86 | 0.000 |

| | | | | | |
|---|---|---|---|---|---|
| Ha*Ha | 1 | 0.0000 | 0.00001 | 0.00 | 0.994 |
| Da*Da | 1 | 3.7911 | 3.79112 | 39.27 | 0.000 |
| Q*Q | 1 | 0.0322 | 0.03225 | 0.33 | 0.576 |
| 2-Way Interaction | 3 | 1.9964 | 0.66548 | 6.89 | 0.008 |
| Ha*Da | 1 | 1.8554 | 1.85536 | 19.22 | 0.001 |
| Ha*Q | 1 | 0.1165 | 0.11645 | 1.21 | 0.298 |
| Da*Q | 1 | 0.0303 | 0.03027 | 0.31 | 0.588 |
| Error | 10 | 0.9655 | 0.09655 | | |
| Lack-of-Fit | 5 | 0.9655 | 0.19310 | * | * |
| Pure Error | 5 | 0.0000 | 0.00000 | | |
| Total | 19 | 15.5699 | | | |

The influence of run circumstances for the dependent variable Nu* may be determined using regression coefficients. The statistical analysis findings are presented in Table 6. The high $R^2$ values for Nu* (93.80%) in Table 6 suggest that this model is acceptable for computing the Nusselt number values, as can be shown from the testing procedures and statistical analysis. It is possible to infer that the model fits well with the experimental data despite the fact that $R^2$-adj quantities for Nu* (88.22% respectively) are smaller than $R^2$.

**7.2. Comparison between means and model estimation:**

The residual plots in Fig. 13. provide the data needed to assess the fitted model correctness. On the *normal probability* plot [26] it is evident that data is primarily scattered along the straight line. The residual histogram also confirms that the residuals are normal. According to this plot of fitted against residual values, the model maximum error is 0.5. These all contribute to the fitted model accuracy within the given co-domain of parameters. Table 5. shows the RSM model's ANOVA accuracy outcomes. If the p-value is less than 0.05, the numerical significance of a parameter is mentioned. The quadratic terms of all three key parameters are not significant. Therefore, those variables are removed from the model. The model coefficient of correlation is determined as 99.98%. This helps to ensure the model accuracy.

According to the response surface methodology (RSM), which yields uncoded units:

$$Nu^{*} = 3.45 + 0.0026\,Ha + 196.1\,Da - 16.8\,\phi - 0.000008\,Ha*Ha - 1580\,Da*Da + 271\,\phi*\phi - 0.602\,Ha*Da - 0.398\,Ha*\phi + 58\,Da*\phi \quad (40)$$

The response variables Nu* are visualised as functions of *Ha, Da* and $\phi$ in Fig.13 using contour residual plots and 3-D surface plots. Fig. 13 (a) demonstrates the influence of Ha and Da on Nu*. The maximum rate of heat transfer (Nu*) is recorded for the middle level of Ha to the higher level of Da. The effect of $\phi$ and Da is depicted in Fig. 13. (b). The greater level of the right middle to left middle level of the whole Da maximises Nu*. It is therefore easiest to transmit heat to the enclosure boundary when Da and $\phi$ are high (see Fig. 13 (c)). Nu* reaches a minimum value, at which point it begins to rise again.

**Table.7. Model Summary**

| S | R-sq | R-sq(adj) | R-sq(pred) |
|---|---|---|---|
| 0.310727 | 93.80% | 88.22% | 45.32% |

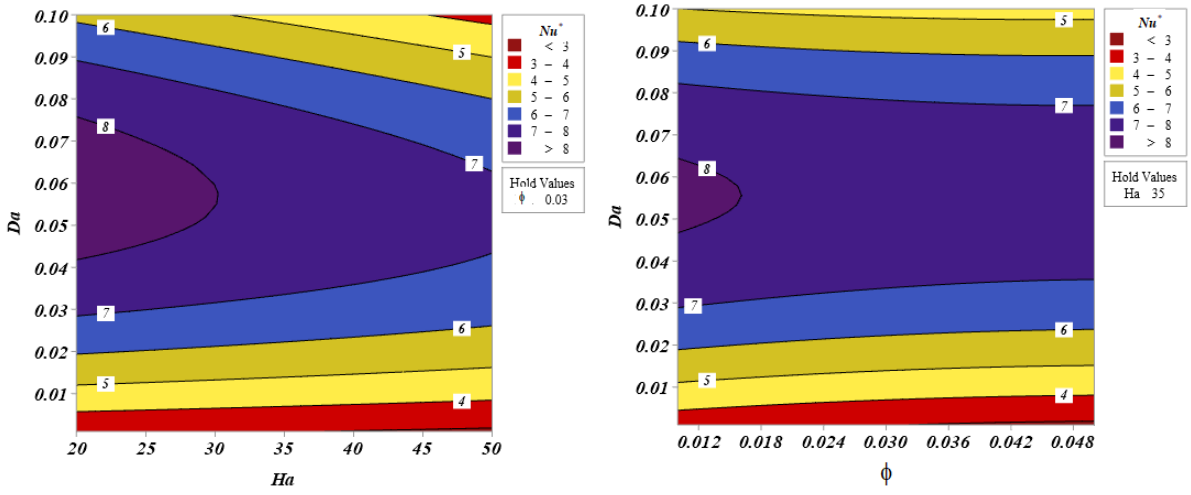


a) b)

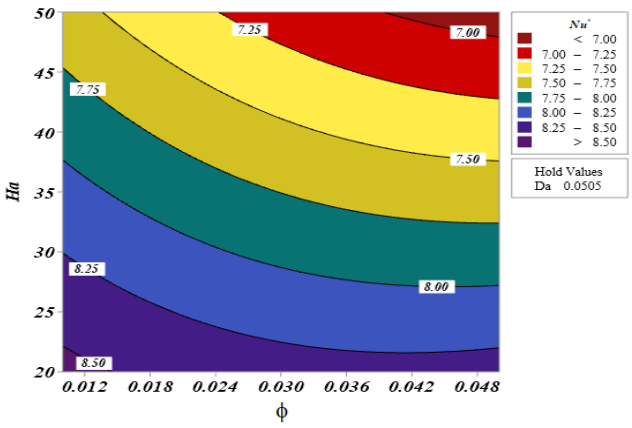


**c)**

**Fig.13.** Contour plot of Nu*

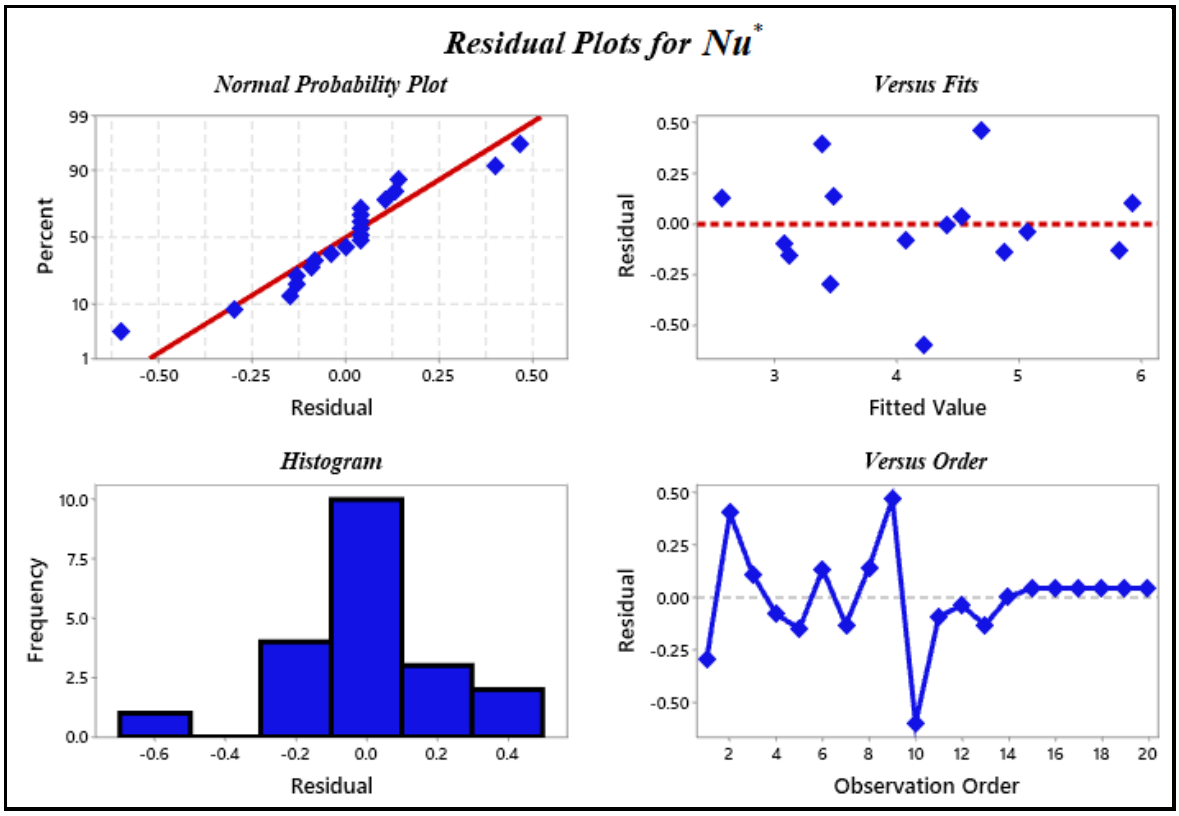


**Fig.14.** Residual plots for *Nu**

### 7.3. Analysis of sensitivity entails

In this section, the heat conversion rate is considered to be a function of temperature. The sensitivity analysis reveals the response variable changes when the key factors increase in importance. The magnitude of sensitivity values at specific levels of the parameters may be

utilized to establish the relative influence of the important components which is beneficial to engineers and designers. A positive correlation follows logically from a positive sensitivity.

The sensitivity total function of the heat transfer rate is calculated as given below:

$$\begin{aligned} Nu^{*} = {} & 3.45 + 0.0026\,Ha + 196.1\,Da - 16.8\,\phi \\ & - 0.000008\,Ha*Ha - 1580\,Da*Da + 271\,\phi*\phi \\ & - 0.602\,Ha*Da - 0.398\,Ha*\phi + 58\,Da*\phi \end{aligned} \tag{41}$$

$$\begin{aligned} \frac{\partial Nu_{avg}}{\partial Ha} &= 0.0026 - 0.000016X_1 - 0.602X_2 - 0.398X_3, \\ \frac{\partial Nu_{avg}}{\partial Da} &= 196.1 - 0.602X_1 - 3160X_2 + 58X_3, \\ \frac{\partial Nu_{avg}}{\partial \phi} &= -16.8 - 0.398X_1 + 58X_2 + 542X_3. \end{aligned} \tag{42}$$

The sensitivity functions are not dependent on Ha. When Ha is at the middle level (Ha = 0), the sensitivity of Nu* to varied amounts of Da and $\phi$ is listed in Table .7. A boost in the response variable occurs when a positive sensitivity value increases the factor variable, and the opposite is also true. Using bar charts the sensitivity may be easily shown. Nu* has a sensitivity seen in Fig.14. Evidently volumetric friction is always a positive sensitivity for Nu. When the Darcy number is low (Da = 0.001), the sensitivity of Nu* to Da is negative for medium levels of volumetric fraction parameter ($\phi$ = 0.01 and 0.03). However, *the sensitivity is positive* when $\phi$ is at an increased level ($\phi$ = 0.05). An increase in the negative sensitivity of Nu* with Da is observed when the level of $\phi$ changes from 0.01 to 0.05. At all levels of $\phi$, the greatest positive sensitivity of Nu* is towards $\phi$ and the greatest positive sensitivity is towards Ha. (Fig. 15(b), When the Darcy number (Da = 0.01) is at the medium level, Ha and Da sensitivities are different. However, the constant positivity sensitivity of Nu* towards $\phi$ is clearly elevated. When the Darcy number is (0.1), Nu* has a constant positive sensitivity to Ha and $\phi$ at all levels (see Fig.15 (c)).

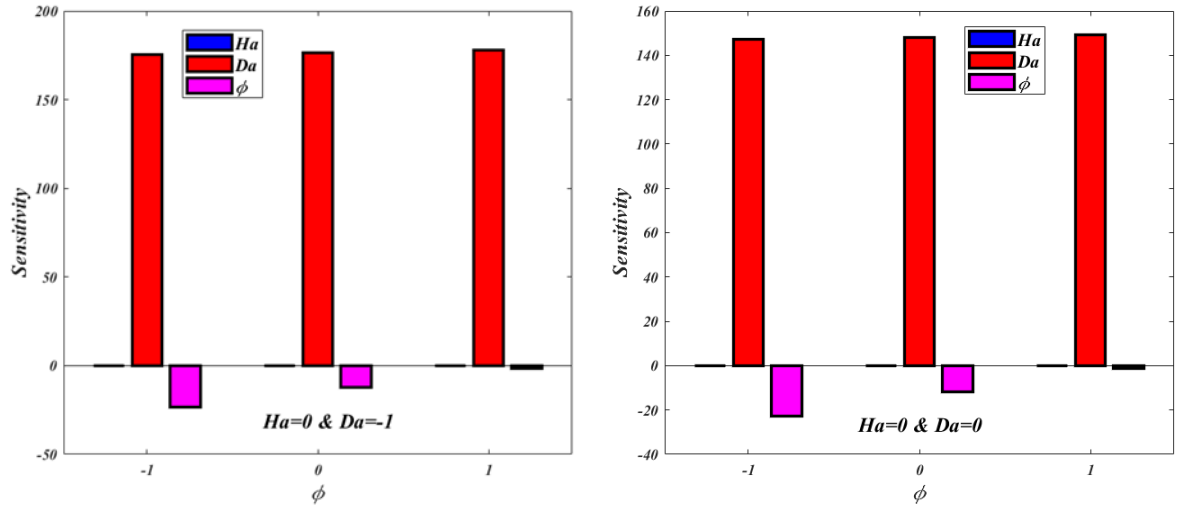


a) b)

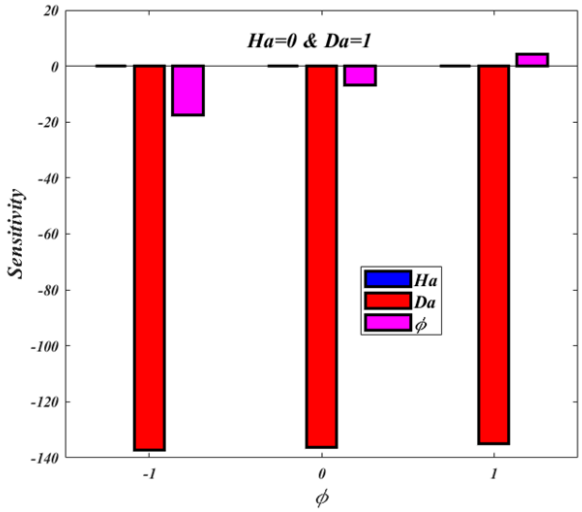


**c)**

**Fig.15. Bar chart showing of sensitivity of Nu***

**Table.7. The Nusselt number (Nu*) of the sensitivity analysis**

| **Order** | **Ha** | **Da** | **Q** | **Sensitivity** | | |
|---|---|---|---|---|---|---|
| | $X_1$ | $X_2$ | $X_3$ | $\frac{\partial Nu_{avg}}{\partial X_1}$ | $\frac{\partial Nu_{avg}}{\partial X_2}$ | $\frac{\partial Nu_{avg}}{\partial X_3}$ |
| 1 | 0 | -1 | -1 | -0.002462 | 175.460 | -23.262 |
| 2 | 0 | -1 | 0 | -0.010422 | 176.620 | -12.422 |
| 3 | 0 | -1 | 1 | -0.018382 | 177.780 | -1.582 |

| | | | | | | |
|---|---|---|---|---|---|---|
| 4 | 0 | 0 | -1 | -0.007880 | 147.020 | -22.740 |
| 5 | 0 | 0 | 0 | -0.015840 | 148.180 | -11.900 |
| 6 | 0 | 0 | 1 | -0.023800 | 149.340 | -1.060 |
| 7 | 0 | 1 | -1 | -0.062060 | -137.380 | -17.520 |
| 8 | 0 | 1 | 0 | -0.070020 | -136.220 | -6.680 |
| 9 | 0 | 1 | 1 | -0.077980 | -135.060 | 4.160 |

## 8. Conclusions

The natural convection in magnetohydrodynamic (MHD) hybrid $TiO_2$-Cu/water nanofluid in a non-Darcy saturated porous medium differential heated cavity has been examined theoretically and numerically with a lattice Boltzmann method. An RSM sensitivity analysis has also been conducted. Tiwari-Das, Maxwell-Garnetts and Brinkman relations have been deployed for the hybrid nanofluid properties. Mesh independence and validation with previous non-magnetic, purely fluid investigations has also been included. The current simulations have shown that:

a) The Nusselt number rises as the Rayleigh number increases whereas it is depleted with elevation in Hartmann number (magnetic field parameter).
b) Increasing Darcy number encourages stronger flow circulation due to the associated larger permeability of the porous medium. It also morphs the isotherm distributions. In addition, the Nusselt number is suppressed at larger values of Darcy number.
c) Based on RSM sensitivity analysis and ANOVA data, a high Darcy number, low nanoparticle volume fraction and low Hartmann number provide the optimum functioning conditions to produce the best wall heat rate (Nusselt number).
d) Nusselt number based on RSM is greatest when the Darcy number is low (Da =0.001).
e) The *maximum* heat transfer rate (Nusselt number) obtained from the statistical RSM experiment by prescribing $Ha=20$, $Da=0.0580$ and $\phi = 0.010$.
f) The *minimum* heat transfer rate is obtained from the statistical experiment by fixing $Ha=50$, $Da=0.001$ and $\phi = 0.050$.

g) The judicious combination of external magnetic field, porous medium permeability and thermal buoyancy effect can be used to successfully manipulate vortex flow characteristics and thermal distributions within enclosures.

The current study has demonstrated that high thermal performance is achievable using magnetic hybrid nanofluids combined with porous media, in for example fuel cells. LBM and RSM have been shown to be powerful numerical tools for simulating complex enclosure flows of nanofluids. However, attention has been restricted to Newtonian nanofluids. Future work may explore non-Newtonian electroconductive hybrid nanofluids.

## Acknowledgements

The authors are grateful to both reviewers for their comments which have served to improve the clarity of the article.

## References

1.S.E. Ahmed, M.A. Mansour, A.M. Rashad, T. Salah, MHD natural convection from two heating modes in fined triangular enclosures filled with porous media using nanofluids, J. Therm. Anal. Calorim. 139 (5) (2020) 3133–3149.

2. X.B. Feng, Q. Liu, Y.L. He, Numerical simulations of convection heat transfer in porous media using a cascaded lattice Boltzmann method, Int. J. Heat Mass Transfer 151 (2020) 119410.

3. M. Izadi, B. Bastani, M.A. Sheremet, Numerical simulation of thermogravitational energy transport of a hybrid nanoliquid within a porous triangular chamber using the two-phase mixture approach, Adv. Powder Technol. 31 (6) (2020) 2493–2504.

4. Venkatadri, K., Bég, O. A., & Prasad, V. R., Numerical simulation of thermal management during natural convection in a porous triangular cavity containing air and hot obstacles. The European Physical Journal Plus, 136 (8) (2021) 1-18.

5. Venkatadri, K., Bég, O. A., & Kuharat, S., Magneto-convective flow through a porous enclosure with Hall current and thermal radiation effects: numerical study. The European Physical Journal Special Topics, 231 (2022) 2555–2568

6. Vedavathi, N., Venkatadri, K., Fazuruddin, S., & Raju, G. S. S., Natural Convection Flow in Semi-Trapezoidal Porous Enclosure Filled with Alumina-Water Nanofluid Using Tiwari and Das' Nanofluid Model. Engineering Transactions. 70 (2022).

7. Venkatadri, K. Radiative magneto-thermogravitational flow in a porous square cavity with viscous heating and Hall current effects: A numerical study of ψ–v scheme. Heat Transfer. 51(7) (2022) 6705-6753.

8. Bég OA, Venkatadri K, Prasad V, et al. Numerical study of magnetohydrodynamic natural convection in a non-Darcian porous enclosure filled with electrically conducting helium gas. Proceedings of the Institution of Mechanical Engineers, Part C: Journal of Mechanical Engineering Science. 236(5) (2022) 2203-2223.

9. S.E. Ahmed, M.A. Mansour, A.M. Rashad, T. Salah, MHD natural convection from two heating modes in fined triangular enclosures filled with porous media using nanofluids, J. Therm. Anal. Calorim. 139 (5) (2020) 3133–3149.

10. F.H. Ali, H.K. Hamzah, M. Mozaffari, S.A.M. Mehryan, M. Ghalambaz, Natural convection of nano encapsulated phase change suspensions inside a local thermal non-equilibrium porous annulus, J. Therm. Anal. Calorim. 141 (5) (2020) 1801–1816.

11 O.R. Alomar, N.M. Basher, A.A. Yousif, Analysis of effects of thermal non-equilibrium and non-Darcy flow on natural convection in a square porous enclosure provided with a heated l shape plate, Int. J. Mech. Sci. 181 (2020) 105704.

12 A.I. Alsabery, T. Tayebi, A.J. Chamkha, I. Hashim, Natural convection of Al2O3-water nanofluid in a non-Darcian wavy porous cavity under the local thermal non-equilibrium condition, Sci. Rep. 10 (1) (2020) 1–22.

13. M. Sheikholeslami, S.A. Shehzad, Numerical analysis of Fe3O4 –H2O nanofluid flow in permeable media under the effect of external magnetic source, Int. J. Heat Mass Transfer 118 (2018) 182–192.

14. M. Sheikholeslami, S.A. Shehzad, CVFEM for influence of external magnetic source on Fe3O4 – H2O nanofluid behavior in a permeable cavity considering shape effect, Int. J. Heat Mass Transfer 115 (2017) 180–191.

15. Mourad, A., Aissa, A., Mebarek-Oudina, F., Jamshed, W., Ahmed, W., Ali, H. M., & Rashad, A. M., Galerkin finite element analysis of thermal aspects of Fe3O4-MWCNT/water hybrid nanofluid filled in wavy enclosure with uniform magnetic field effect. International Communications in Heat and Mass Transfer, 126, (2021)105461.

16. Dogonchi, A. S., Tayebi, T., Karimi, N., Chamkha, A. J., & Alhumade, H., Thermal-natural convection and entropy production behavior of hybrid nanoliquid flow under the effects of magnetic field through a porous wavy cavity embodies three circular cylinders. *Journal of the Taiwan Institute of Chemical Engineers, 124*, (2021)162-173.

17. M. Muneeshwaran, G. Srinivasan, P. Muthukumar, and C. C. Wang, "Role of hybrid-nanofluid in heat transfer enhancement – A review," Int. Commun. Heat Mass Transf., 125 (2021) 105341.

18. Ozoe H, Okada K. The effect of the direction of the external magnetic field on the three-dimensional natural convection in a cubical enclosure. Int J Heat Mass Transfer. 1989;32(10):1939–1954.

19. Biswas N, Sarkar UK, Chamkha AJ, et al. Magneto-hydrodynamic thermal convection of Cu–Al2O3/water hybrid nanofluid saturated with porous media subjected to half-sinusoidal nonuniform heating. J Therm Anal Calorim. 2021; 143:1727–1753.

20. Biswas N, Manna NK, Chamkha AJ. Effects of half-sinusoidal nonuniform heating during MHD thermal convection in Cu–Al2O3/water hybrid nanofluid saturated with porous media. J Therm Anal Calorim. 2021; 143:1665–1688.

21. Al-Balushi LM, Rahman MM. Convective heat transfer utilizing magnetic nanoparticles in the presence of a sloping magnetic field inside a square enclosure. J Thermal Sci Eng Appl. 2019; 11:041013-1–19.

22. Mehryan SAM, Izadi M, Chamkha AJ, et al. Natural convection and entropy generation of a ferrofluid in a square enclosure under the effect of a horizontal periodic magnetic field. J Mol Liq. 2018; 263:510–525.

23. Rahimi A, Sepehr M, Lariche MJ, Kasaeipoor A, Malekshah EH, Kolsi L. Entropy generation analysis and heatline visualization of free convection in nanofluid (KKL model-

based)-filled cavity including internal active fins using lattice Boltzmann method. Computers & Mathematics with Applications. 2018;75(5):1814-30.

24. N. H. Khan, M. K. Paswan, and M. A. Hassan, “Natural convection of hybrid nanofluid heat transport and entropy generation in cavity by using Lattice Boltzmann Method,” J. Indian Chem. Soc., vol. 99, no. 3, p. 100344, 2022, doi: 10.1016/j.jics.2022.100344.

25. H. Sajjadi, A. A. Delouei, R. Mohebbi, M. Izadi, and S. Succi, “Natural convection heat transfer in a porous cavity with sinusoidal temperature distribution using Cu/Water nanofluid: double MRT Lattice Boltzmann method,” Commun. Comput. Phys., vol. 29, no. 1, pp. 292–318, 2020, doi: 10.4208/CICP.OA-2020-0001.

26. M. R. Safaei, A. Karimipour, A. Abdollahi, and T. K. Nguyen, “The investigation of thermal radiation and free convection heat transfer mechanisms of nanofluid inside a shallow cavity by lattice Boltzmann method,” Phys. A Stat. Mech. its Appl., vol. 509, pp. 515–535, 2018.

27. M. Ghalambaz, M.A. Sheremet, S. Mehryan, F.M. Kashkooli, I. Pop, Local thermal non-equilibrium analysis of conjugate free convection within a porous enclosure occupied with Ag–MgO hybrid nanofluid, J. Therm. Anal. Calorim. 135 (2) (2019) 1381–1398.

28. S. Mehryan, M. Ghalambaz, A.J. Chamkha, M. Izadi, Numerical study on natural convection of Ag–MgO hybrid/water nanofluid inside a porous enclosure: A local thermal non-equilibrium model, Powder Technol. 367 (2020) 443–455.

29. I. V. Miroshnichenko, M. A. Sheremet, H. F. Oztop, and N. Abu-Hamdeh, “Natural convection of Al2O3/H2O nanofluid in an open inclined cavity with a heat-generating element,” Int. J. Heat Mass Transf., vol. 126, pp. 184–191, 2018, doi: 10.1016/j.ijheatmasstransfer.2018.05.146

30. S. Ahmad Khan, M. I. Khan, T. Hayat, M. Faisal Javed, and A. Alsaedi, “Mixed convective non-linear radiative flow with TiO2-Cu-water hybrid nanomaterials and induced magnetic field,” Int. J. Numer. Methods Heat Fluid Flow, vol. 29, no. 8, pp. 2754–2774, 2019, doi: 10.1108/HFF-12-2018-0748

31. T. A. Yusuf, F. Mabood, W. A. Khan, and J. A. Gbadeyan, “Irreversibility analysis of Cu-TiO2-H2O hybrid-nanofluid impinging on a 3-D stretching sheet in a porous medium with nonlinear radiation: Darcy-Forchhiemer’s model,” Alexandria Eng. J., vol. 59, no. 6, pp. 5247–5261, 2020, doi: 10.1016/j.aej.2020.09.053

32. R. Nath and K. Murugesan, “Double diffusive mixed convection in a Cu-Al2O3/water nanofluid filled backward facing step channel with inclined magnetic field and part heating load conditions,” J. Energy Storage, vol. 47, no. October 2021, p. 103664, 2022, doi: 10.1016/j.est.2021.103664

33. S. A. M. Mehryan, F. M. Kashkooli, M. Ghalambaz, and A. J. Chamkha, “Free convection of hybrid Al2O3-Cu water nanofluid in a differentially heated porous cavity,” Adv. Powder Technol., vol. 28, no. 9, pp. 2295–2305, 2017, doi: 10.1016/j.apt.2017.06.011

34. Z. Abdelmalek et al., “Mixed radiated magneto Casson fluid flow with Arrhenius activation energy and Newtonian heating effects: Flow and sensitivity analysis,” Alexandria Eng. J., vol. 59, no. 5, pp. 3991–4011, 2020, doi: 10.1016/j.aej.2020.07.006.

35. Selimefendigil, Fatih, and Hakan F. Öztop., Thermal management and performance improvement by using coupled effects of magnetic field and phase change material for hybrid nanoliquid convection through a 3D vented cylindrical cavity., International Journal of Heat and Mass Transfer 183 (2022): 122233.

36. Kumar, S., Gangawane, K.M. & Oztop, H.F. Applications of lattice Boltzmann method for double-diffusive convection in the cavity: a review. J Therm Anal Calorim 147, 10889–10921 (2022). https://doi.org/10.1007/s10973-022-11354-z

37. Alshuraiaan, B., Izadi, M. and Sheremet, M.A. ‘Numerical study on charging performance of multi-enclosed thermal storage: Multiple versus integrated thermal storage’, *Case Studies in Thermal Engineering*. Elsevier Ltd, 33(2022), p. 101954. doi: 10.1016/j.csite.2022.101954.

38. Alshuraiaan, B., Shahrestani, A. B. and Izadi, M. ‘Numerical study on passive parameters of a fluid-solid interaction problem derived by natural convection in a circular enclosure’, *Alexandria Engineering Journal*. Faculty of Engineering, Alexandria University, (2023)63, pp.415-426. Doi: 10.1016/j.aej.2022.07.057.

39. Fadaei, M. ‘Conjugated non- Newtonian phase change process in a shell and tube heat exchanger: A parametric-geometric analysis’, *Applied Thermal Engineering*. Elsevier Ltd, (2023) 220, p. 119795. doi:10.1016/j.applthermaleng.2022.119795.

40. Huu-Quan, D. ‘3D numerical investigation of turbulent forced convection in a double-pipe heat exchanger with flat inner pipe’, *Applied Thermal Engineering*. Elsevier Ltd, 182(2021), p. 116106. doi:10.1016/j.applthermaleng.2022. 116106.

41. Izadi, M. ‘Effects of porous material on transient natural convection heat transfer of nano-fluids inside a triangular chamber’, *Chinese Journal of Chemical Engineering*. Elsevier B. V., (2020) 28(5), pp.1203-1213. doi:10.1016/j.cjche.2020.01.021.

42. Izadi, M., Hajjar., Alshehri, H. M., Saleem, A., ‘Analysis of applying fin for charging process of phase change material inside H-shaped thermal storage’, *International Communications in Heat and Mass Transfer*. Elsevier Ltd, 139(2022), p. 106421. doi:10.1016/j.icheatmasstransfer.2022.106421

43. Izadi, M., Hajjar., Alshehri, H. M., Sheremet, M., ‘Charging process of a partially heated trapezoidal thermal energy storage filled by nano-enhanced PCM using controlable uniform magnetic field’, *International Communications in Heat and Mass Transfer*. Elsevier Ltd, 138(2022), p. 106349. doi:10.1016/j.icheatmasstransfer.2022.106349.

44. Izadi, M., Fagehi, H., ‘Influence of finned charges on melting process performance in a thermal energy storage’, *Thermal Science and Engineering Progress*. Elsevier Ltd, 37(2022), p. 101547. doi: 10.1016/j.tsep.2022.101547.

45. Izadi, M., Bastani, B. and Sheremet, M. A. ‘Numerical simulation of thermogravitational energy transport of a hybrid nanoliquid within a porous triangular chamber using the two-phase mixture approach’, *Advanced Powder Technology*. 31(6), (2020) pp. 2493-2504. doi:10.1016/j.apt.2022.04.011.

46. Sajjadi, H. ‘Natural convection heat transfer in a porous cavity with sinusoidal temperature distribution using Cu/Water nanofluid: Double MRT lattice Boltzmann method’, *Communications in Computational Physics*, 29(1), (2020) pp. 292-318. doi:10.4208/CICP.OA-2020-001.

47. Shehzad, S. A. ‘Influence of fin orientation on the natural convection of aqueous-based nano-encapsulated PCMs in a heat exchanger equipped with wing-like fins’, *Chemical*

*Engineering and Processing - Process Intensification*. 160(2021), p. 108287. doi:10.1016/j.cep.2020.108287.

48. Xiong, Q, 'State-of-the-art review of nanofluids in solar collectors: A review based on the type of the dispersed nanoparticles', *Journal of Cleaner Production*. Elsevier Ltd, 310(2021), p. 127528. Doi:10.1016/j.jclepro.2021.127528.

49. Chu, Y. M. 'Examining rheological behavior of MWCNT-$TiO_2$/5W40 hybrid nanofluid based on experiments and RSM/ANN modelling', *Journal of Molecular Liquids*. Elsevier B. V., 333, (2021) p.115969. doi:10.1016/j.molliq.2021.115969.

50. Chu, Y. M., Bilal, S. and Hajizadeh, M. R. 'Hybrid ferrofluid along with MWCNT for augmentation of thermal behavior of fluid during natural convection in a cavity', *Mathematical Methods in the Applied Sciences,* (2020), pp. 1-12. doi:10.1002/mma.6937.

51. Ibrahim, M., Saeed, T., Algehyne, E. A., Alsulami, H., 'Optimization and effect of wall conduction on natural convection in a cavity with constant temperature heat source: Using lattice Boltzmann method and neural network algorithm', *Journal of Thermal Analysis and Calorimetry*. (2021) 144(6), pp. 2449-2463. doi:10.1007/s10973-021-10654-0.

52. Ibrahim, M., Saeed, T., Alshehri, A. M., 'The numerical simulation and sensitivity analysis of a non-Newtonian fluid flow inside a square chamber exposed to a magnetic field using the FDLBM approach', *Journal of Thermal Analysis and Calorimetry*. Springer International Publishing, (2021)144(6), pp. 2403-2421. Doi:10.1008/s10973-021-10695-5.

53. Abbas, A. 'Computational study of the coupled mechanism of thermophoretic transportation and mixed convection flow around the surface of a sphere', *Molecules*, (2020) 25(11). doi:10.3390/molecules25112694.

54. Ashraf, M, 'Computational analysis of the effect of nano particle material motion on mixed convection flow in the presence of heat generation and absorption', *Computers, Materials and Continua,* (2020) 65(2), pp. 1809-1823. doi:10.32604/cmc.2020.011404.

55. Ullah, Z. 'Computational analysis of the oscillatory mixed convection flow along a horizontal circular cylinder in thermally stratified medium', *Computers, Materials and Continua,* (2020) 65(1), pp. 102-123.

56. K. Venkatadri & O. Anwar Bég, Lattice Boltzmann simulation of thermomagnetic natural convection in an enclosure partially filled with a porous medium, *Waves in Random and Complex Media* (2022). https://doi.org/10.1080/17455030.2022.2157516